Characterization and Correction of Relative Humidity Measurements from Vaisala RS80-A Radiosondes at Cold Temperatures

Larry M. Miloshevich

National Center for Atmospheric Research/MMM, Boulder, Colorado*

Holger Vömel

National Oceanic and Atmospheric Administration, Boulder, Colorado

Ari Paukkunen

Vaisala Oy, Helsinki, Finland

Andrew J. Heymsfield

National Center for Atmospheric Research/MMM, Boulder, Colorado*

Samuel J. Oltmans

National Oceanic and Atmospheric Administration, Boulder, Colorado

(Manuscript received 11 October 1999, in final form 4 April 2000)

ABSTRACT

Radiosonde relative humidity (RH) measurements are known to be unreliable at cold temperatures. This study characterizes radiosonde RH measurements from Vaisala RS80-A thin-film capacitive sensors in the temperature range 0° to −70°C. Sources of measurement error are identified, and two approaches for correcting the errors are presented. The corrections given in this paper apply only to the Vaisala RS80-A sensor, although the RS80-H sensor is briefly discussed for comparison.

A temperature-dependent correction factor is derived from statistical analysis of simultaneous RH measurements from RS80-A radiosondes and the NOAA cryogenic frostpoint hygrometer. The mean RS80-A measurement error is shown to be a dry bias that increases with decreasing temperature, and the multiplicative correction factor is about 1.3 at −35°C, 1.6 at −50°C, 2.0 at −60°C, and 2.4 at −70°C. The fractional uncertainty in the mean of corrected measurements, when large datasets are considered statistically, increases from 0.06 at 0°C to 0.11 at −70°C. The fractional uncertainty for correcting an individual sounding is about ±0.2, which is larger because this statistical approach considers only the mean value of measurement errors that are not purely temperature dependent. The correction must not be used outside the temperature range 0° to −70°C, because it is a meaningless extrapolation of a polynomial curve fit.

Laboratory measurements of sensor response conducted at Vaisala are used to characterize some of the individual sources of RS80-A measurement error. A correction factor is derived for the dominant RS80-A measurement error at cold temperatures: an inaccurate approximation for the sensor's temperature dependence in the data processing algorithm. The correction factor for temperature-dependence error is about 1.1 at −35°C, 1.4 at −50°C, 1.8 at −60°C, and 2.5 at −70°C. Dependences and typical magnitudes are given for measurement errors that result from the temperature dependence of the sensor's time constant, and from several smaller bias errors and random uncertainties.

1. Introduction

Inaccuracies in radiosonde relative humidity (RH) measurements at cold temperatures are not generally a serious detriment to their common operational use in weather forecasting. Prior to 1993, the U.S. National Weather Service (NWS) did not even report RH measurements below −40°C because they were known to be unreliable (Ross and Elliott 1996). However, interest by the research community in obtaining accurate RH measurements in the mid- and upper troposphere has increased in recent years. Studies of climate-related issues require accurate RH measurements in the upper troposphere (UT) for such applications as validating retrievals of water vapor concentrations from ground-based and satellite remote sensors, initializing numerical

Corresponding author address: Dr. Larry M. Miloshevich, National Center for Atmospheric Research/MMM, P.O. Box 3000, Boulder, CO 80307-3000.
E-mail: milo@ucar.edu

models, improving radiative transfer algorithms, constructing water vapor climatologies, and ascertaining the meteorological conditions that lead to the formation of cirrus clouds and aircraft contrails.

Existing archives of upper-tropospheric radiosonde RH data are not well suited for climate change studies, due in part to historical variability in quality control procedures and reporting practices among stations (Elliott and Gaffen 1991), and also to measurement biases introduced by radiosondes from different manufacturers whose sensor construction and data reduction algorithms differ substantially and have changed over time (e.g., Gaffen 1993; Wade 1995). For instance, until recently the NWS arbitrarily reported all measurements below 20% RH[1] as a dewpoint depression of 30°C, which would introduce a dry bias into the radiosonde climatological record if interpreted as a legitimate value (Ross and Elliott 1996). A series of World Meteorological Organization (WMO)-sponsored intercomparisons of radiosonde humidity measurements (e.g., Ivanov et al. 1991) showed that, although variability between radiosondes of the same manufacturer were small, large discrepancies were seen between radiosondes of different manufacturers. Few studies have been conducted to assess the absolute accuracy of operational radiosonde RH data at cold temperatures.

A comparison of global radiosonde water vapor measurements in the UT using retrievals from Television Infrared Observational Satellite (TIROS) Operational Vertical Sounder (TOVS) radiance measurements as a fixed reference (Soden and Lanzante 1996) found large discrepancies that often fell along geopolitical boundaries of countries using radiosondes from different manufacturers. Relative to the satellite retrievals, thin-film capacitive sensors (mainly Vaisala) and carbon hygristor sensors (mainly VIZ) both exhibited a mean dry bias of about 10% RH (with considerable scatter about the mean). Regional variations in water vapor were found to agree well with the retrievals when this systematic bias was removed. Similarly, a comparison of RH measurements in the UT from Vaisala RS80-A and AIR radiosondes with water vapor retrievals from Geostationary Operational Environmental Satellite (GOES) radiance measurements and from ground-based Raman lidar measurements (Soden et al. 1994) showed a systematic dry bias for both types of radiosondes relative to the satellite retrievals. The mean dry bias was 5% RH for dry conditions and 10% RH for moist conditions, whereas the lidar retrievals showed an average moist bias of about 3% RH relative to the satellite retrievals. The agreement between time series of the radiosonde measurements and the satellite retrievals improved markedly when the mean dry bias in the radiosonde data

was removed. It should be noted that comparison of radiosonde point measurements with the altitude-weighted and volume-averaged retrievals from satellites is complicated by the substantial spatial and temporal variability of atmospheric RH. Collocation and representativeness errors in such comparisons may exceed the measurement errors (Kitchen 1989).

It is more difficult for radiosonde sensors to accurately measure RH in the UT than at lower altitudes because the measurement depends on the rapid exchange of water molecules between the sensor and the air, and water vapor concentrations decrease by several orders of magnitude between the surface and the tropopause. The accuracy and reliability of radiosonde RH measurements are generally thought to decrease as the water vapor concentration, temperature, or pressure decreases (Elliott and Gaffen 1991). Radiosonde RH measurements in the stratosphere are considered to be essentially useless (WMO 1996; Schmidlin and Ivanov 1998), in part because uncertainty in the measurement generally exceeds typical stratospheric humidities of a few percent RH.

Manufacturers' specifications do not necessarily represent the accuracy of operational radiosonde measurements in the UT because the specifications, as well as the sensor calibrations, usually correspond to temperatures above 0°C, where most sensors perform well. Measurements at temperatures other than the calibration temperature are typically adjusted using an algorithm that describes the temperature dependence of a specific sensor type. Rigorous calibration of individual sensors over a wide temperature range is too expensive for the operational radiosonde market. The accuracy of radiosonde RH measurements in the UT therefore depends in part upon the accuracy and generality of the temperature-dependence algorithm used in the data processing. Measurement errors by both thin-film capacitive and carbon hygristor sensors were reported to increase with decreasing temperature during the laboratory phase of a recent WMO radiosonde intercomparison (Balagurov et al. 1998). Lorenc et al. (1996) found that RH measurements from both Vaisala and VIZ radiosondes exhibited a dry bias in the UT that, when assimilated into a Numerical Weather Prediction model, led to underprediction of clouds and precipitation because fractional cloud cover in the model is very sensitive to the RH field.

The response time of radiosonde RH sensors is not an accuracy issue in a test or calibration chamber, because the sensor is allowed to equilibrate. However, operational measurements are degraded when the sensor time constant becomes so long that it cannot adequately respond to changes in atmospheric RH at typical radiosonde ascent rates. Blackmore and Taubvurtzel (1999) conducted chamber tests of carbon hygristor sensors used by the NWS and found that the sensors responded extremely slowly at cold temperatures and no longer functioned at all when the temperature was near −60°C

---

[1] All values of RH in this paper are given with respect to liquid water, including the RH corresponding to ice saturation (the saturation humidity over ice).

or colder. The time constant (63% response time) of the Vaisala RS80-A and RS80-H thin-film capacitive sensors was reported to increase with decreasing temperature, exceeding 1 min at temperatures colder than about −50°C (Antikainen and Paukkunen 1994; Paukkunen 1995).

The intent of this paper is to characterize RH measurements from Vaisala RS80-A radiosondes, currently the most frequently used radiosonde in the world, and to develop corrections for measurement errors in the temperature range from 0° to −70°C. A temperature-dependent correction factor is derived from statistical analysis of a dataset of simultaneous RH measurements from RS80-A radiosondes and the National Oceanic and Atmospheric Administration (NOAA) cryogenic frost-point hygrometer. Although these are operational measurements rather than a controlled intercomparison, the use of the hygrometer as an in situ measurement standard improves upon studies in which radiosondes are compared only to each other (e.g., Schmidlin and Ivanov 1998), primarily because the hygrometer's calibration uncertainty is not temperature dependent and its response time at cold temperatures is relatively fast. The framework for a second correction approach is also presented, using laboratory measurements conducted at Vaisala to identify and characterize the individual sources of RS80-A measurement error. A correction for the single largest source of RS80-A measurement error at cold temperatures is derived. An overview of RS80-A measurement characteristics at cold temperatures is given in section 2, and the design and measurement uncertainties for the RS80-A and the NOAA hygrometer are summarized in section 3. A correction for RS80-A data is derived from the RS80-A/hygrometer dataset in section 4, and individual RS80-A measurement errors are characterized in section 5. A sample application of the corrections is shown in section 6, and conclusions are given in section 7.

The corrections developed in this paper apply only to Vaisala RS80-A radiosondes, not to radiosonde RH measurements in general, and specifically not to the Vaisala RS80-H. The RS80-A was introduced in about 1980 and the RS80-H in 1993, and both use the Humicap thin-film capacitive sensors. The two Vaisala sensors differ primarily in the chemical composition and properties of the sensor dielectric material, and in the accuracy of the data processing algorithm that describes the sensor's temperature dependence. In 1999 about three-fourths of Vaisala radiosondes produced were the RS80-A, although the RS80-H is widely used in Canada, England, Australia, Ireland, and in the United States, by the NWS and various research programs. Processed data from the RS80-A and RS80-H cannot be distinguished from each other, but several means of identifying the RS80-A are described in appendix A.

2. RS80-A measurement characteristics

This study was initiated because RS80-A measurements within cirrus clouds during the 1991 National

Aeronautics and Space Administration (NASA)/First International Satellite Cloud Climatology Project (ISCCP) Regional Experiment-II (FIRE-II) always reported RH values that were substantially below ice saturation. The measurements were inconsistent with detailed ice crystal characteristics measured simultaneously by the National Center for Atmospheric Research (NCAR) balloon-borne Formvar replicator, a cloud particle sampling instrument that preserves ice crystals as plastic replicas (Miloshevich and Heymsfield 1997). The ice crystals in the upper levels of the clouds had pristine crystalline shapes with sharp edges, indicating active crystal growth in an ice-supersaturated environment (Heymsfield and Miloshevich 1995).

Profiles of RH measured simultaneously by the NOAA cryogenic frostpoint hygrometer and two RS80-A radiosondes in a cirrus cloud are shown in Fig. 1, with superimposed ice crystals that were measured simultaneously by the replicator and are representative of the cloud column. Sharp-edged ice crystals in the upper levels of the cloud are consistent with the measurement of ice supersaturation by the hygrometer, and the rounded and sublimating crystals in the lower levels of the cloud are consistent with the measurement of ice subsaturation. Radiosonde sensors in general cannot measure ice supersaturation because the surface of the sensor acts as a nucleation site upon which vapor condenses, so the sensor itself is actually exposed to air that is at ice saturation. However, both RS80-A sensors measure 25%–30% RH below ice saturation when the hygrometer measures ice supersaturation. The close agreement between the two RS80-A sensors suggests an error in the sensor calibration. Within the ice-supersaturated region of the cloud, the error relative to the ice-saturation curve is a dry bias, the magnitude of which increases with decreasing temperature. However, both radiosondes agree very closely with the hygrometer between 9- and 10-km altitudes where the air is dry, suggesting that the measurement error also depends on the RH. All three instruments detect the same structure in the RH profile below 10 km. The slower time response of the RS80-A relative to the hygrometer is apparent between 10- and 10.5-km altitude, where the RH increases rapidly.

Figure 2 shows the dataset of simultaneous RS80-A and hygrometer measurements that is used in section 4 to derive a correction for RS80-A data. The existence of high ice supersaturations in the atmosphere as measured by the hygrometer (Fig. 2a) is consistent with previous findings from numerical calculations, airborne cryogenic hygrometer measurements (Heymsfield and Miloshevich 1993, 1995), and airborne diode laser hygrometer measurements (Heymsfield et al. 1998). The RS80-A measurements rarely reached ice saturation at temperatures below −40°C (Fig. 2b), and the maximum RH values are below ice saturation by an amount that increases with decreasing temperature. These data were measured on both the ascent and descent portions of the
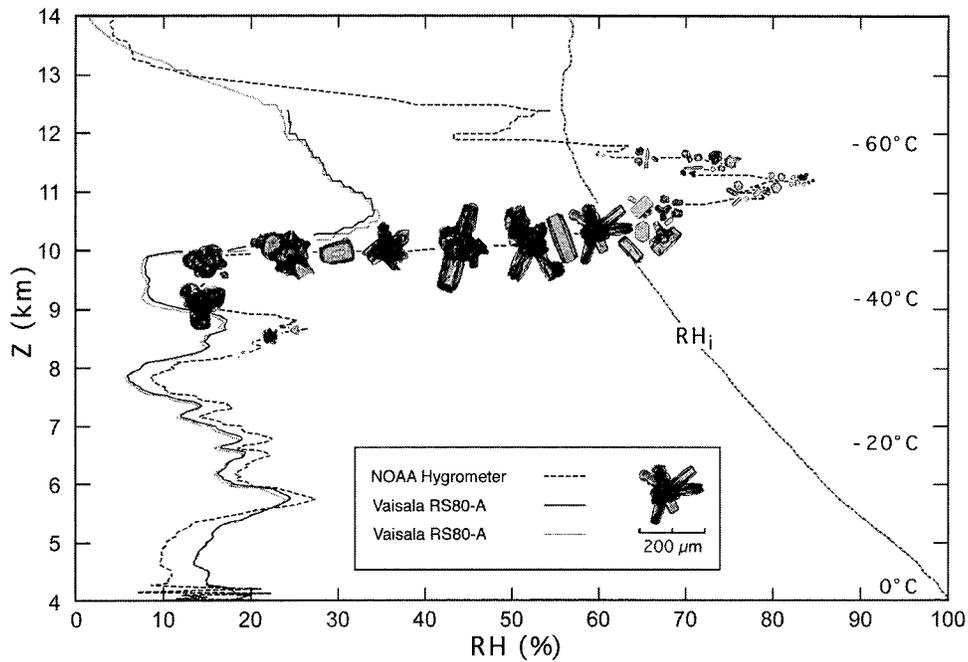
Fig. 1. Altitude profiles of RH (with respect to liquid water) measured simultaneously by the NOAA cryogenic frostpoint hygrometer and two Vaisala RS80-A radiosondes in a cirrus cloud on 10 Nov 1994 near Boulder, Colorado. Superimposed ice crystals measured simultaneously by the NCAR balloon-borne Formvar replicator show the cloud microphysical properties. An ice-saturation curve (RH_i) and several reference temperatures are also shown.

flights, and the artificial-looking contrast in the density of points at $-30°C$ results from combining data from the ascent portions at temperatures colder than $-30°C$ with data from the descent portions at temperatures warmer than $-30°C$, for reasons discussed in detail in section 4.

Figure 3 shows trends in the RS80-A measurements with temperature and RH, relative to the hygrometer measurements. RS80-A measurements from Fig. 2 are

plotted in Fig. 3 only if the corresponding hygrometer measurement was within a specified range of RH. Figure 3a shows the subset of RS80-A measurements when the corresponding hygrometer measurement was in the interval between ice saturation (RH_i) and $RH_i - 10\%$. Comparison of the mean hygrometer measurements (represented by the dotted line) with the mean of the corresponding RS80-A measurements (represented by the jagged line or the associated curve fit) shows that
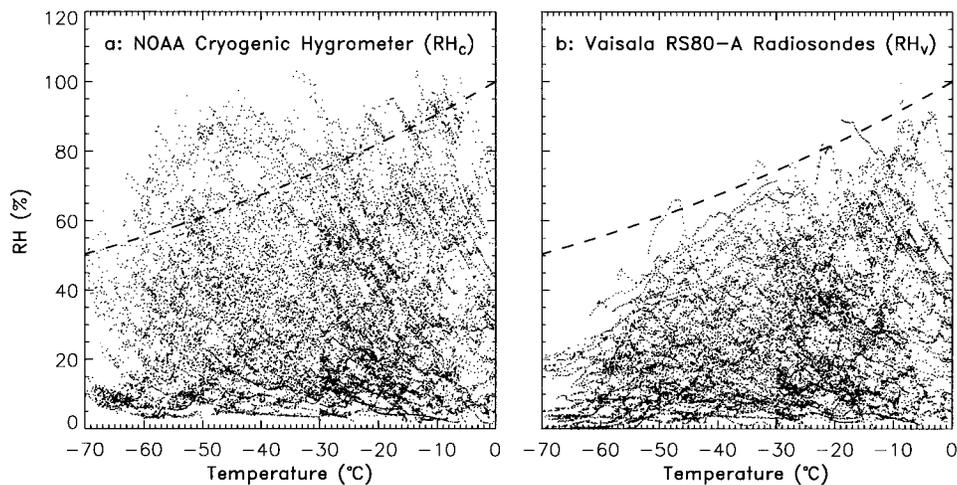

Fig. 2. Dataset of simultaneous RH measurements from the NOAA hygrometer and Vaisala RS80-A radiosondes. Dashed curve is ice saturation.
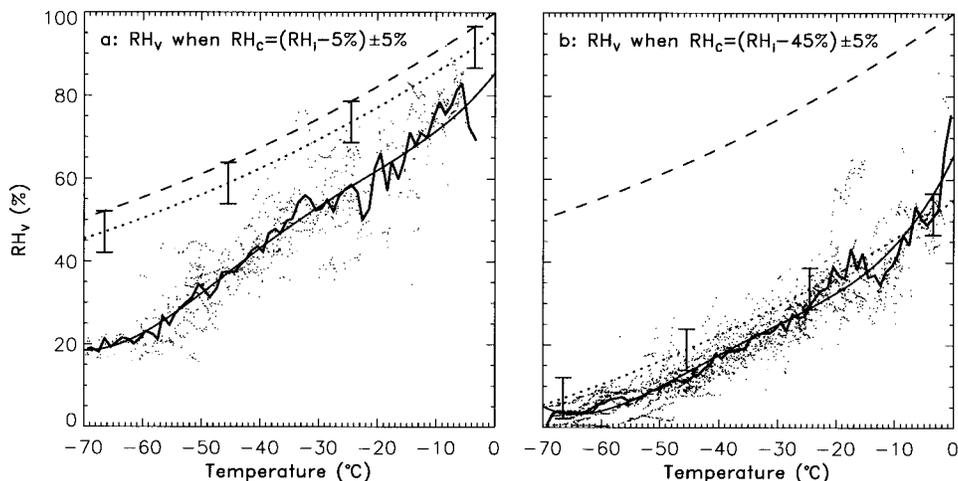
FIG. 3. Subset of Vaisala RS80-A measurements from Fig. 2 (RH_v) for all instances when the corresponding cryogenic hygrometer measurement (RH_c) was within the indicated ±5% RH range centered on the dotted curve and bounded by the vertical bars. Dashed curve is ice saturation (RH_i). Also shown are the mean of the selected RH_v data in each 1°C temperature bin (jagged curve) and a polynomial fit to the RH_v data (solid curve).

on average the RS80-A exhibits a dry bias relative to the hygrometer by an amount that increases with decreasing temperature. This temperature-dependent bias is also seen for the drier conditions in Fig. 3b, but the magnitude of the bias is less than the bias for the moister conditions in Fig. 3a, indicating that the average RS80-A measurement error increases with increasing RH as well as with decreasing temperature.

3. Instrumentation

a. RS80-A sensor principles and calibration

The Vaisala Humicap RH sensors are thin-film capacitive sensors, the temperature-compensated capacitance of which is proportional to the ambient water vapor concentration. The sensor consists of a highly porous electrode through which water molecules diffuse into a thin polymer layer on a glass substrate. Water molecules are captured at binding sites within the polymer structure in concentrations proportional to the ambient water vapor density, which alters the capacitance of the polymer. This capacitance is measured by the radiosonde and then converted to RH (with respect to liquid water) by the data processing system, based on the calibration described below. Additional description of the sensor is given by Paukkunen (1995) and Antikainen and Paukkunen (1994).

The chemical properties of the polymer are largely responsible for the characteristics of capacitive RH sensors (Sakai et al. 1996; Matsuguchi et al. 1998). These characteristics include molecular selectivity (susceptibility to contamination by nonwater molecules), stability (e.g., drift and hysteresis), and sensitivity (time response). Hysteresis and drift occur when clusters of water molecules form because too many hydrophilic sorp-

tion sites are present in the polymer structure (Sakai et al. 1996), and freezing of clustered water molecules in poor-quality sensor polymers renders them useless. Water molecules in the polymer used by Vaisala are inferred to be present mainly as individual molecules rather than as clusters, based on measurements of the heat of sorption conducted at Vaisala, which indicated that no phase change occurs.

The electrical response of the sensors to water vapor is inherently a nonlinear function of both the ambient temperature and the ambient RH. The RH dependence of the sensor response is well behaved throughout the range 0%–100% RH (or to ice saturation at temperatures below 0°C), so the calibrated sensors are capable of measuring both very dry and very moist conditions.

The Vaisala procedure for sensor calibration uses general calibration models, which give the mean RH dependence and temperature dependence of the sensor response for a given sensor type (e.g., RS80-A or RS80-H). The general calibration curves are then adjusted according to an individual calibration of each sensor at +20°C and at 0% and 75% RH, and the individual calibration is checked against quality-control criteria at −30°C and +45°C at the ambient RH. The general calibration models were developed by measuring the response of a sample of sensors over the full range of humidity (0% RH to either water saturation above 0°C or ice saturation below 0°C) and over a broad temperature range (+60° to −90°C). The general humidity model gives the RH dependence of the sensors, and the temperature dependence is given by two calibration curves: the baseline temperature dependence at 0% RH and the temperature dependence at saturation. The individual calibration of each sensor is used to adjust the general humidity model at +20°C to compensate

for the small production variabilities in individual sensors that were averaged together in developing the general humidity model. A measured sensor capacitance at a given temperature is converted to RH in the data processing by interpolation along the adjusted humidity model, the endpoints of which are fitted between the two temperature-dependence curves at the measured temperature. The coefficients of the individually adjusted humidity model and the temperature-dependence curves are delivered with the radiosonde.

b. Sources of RS80-A measurement error

1) TEMPERATURE-DEPENDENCE ERROR

The temperature-dependence coefficients delivered with the RS80-A describe a *linear* function of temperature, which is only an approximation to the actual nonlinear temperature dependence of the sensors. The linear approximation leads to a temperature-dependent error that increases substantially with decreasing temperature below about $-30°C$. Temperature-dependence error is not a limitation of the sensor but is a consequence of the data processing algorithm. A linear temperature dependence was originally chosen by Vaisala because it was sufficiently accurate for the temperature range commonly of interest to radiosonde users at the time, and a linear temperature dependence was also needed to maintain the utility of older sounding systems. However, the temperature-dependence error is substantial at the colder temperatures of recent interest for climate-related research. A correction for temperature-dependence error is developed in section 5. The linear temperature-dependence coefficients will not be changed by Vaisala for two reasons: a more accurate nonlinear temperature dependence is used for the newer RS80-H and RS90-H sensors, and it would be difficult and costly to modify all RS80-A data acquisition systems in use throughout the world.

2) TIME-LAG ERROR

The sensor calibration procedure and the calibration models represent steady-state measurement conditions, whereas operationally the sensor responds with a time constant that increases exponentially with decreasing temperature. At cold temperatures the sensor is unable to respond quickly to changes in the ambient RH, leading to a time-lag error that smooths the ambient RH profile and decreases the scale of details that can be resolved. The magnitude of time-lag error depends on the temperature dependence of the time constant and on the rate of change of atmospheric RH during a sounding. The sensor time constant reflects the rate at which water molecules diffuse into and out of the sensor polymer, and its temperature dependence mainly results from the absorption and desorption characteristics of the polymer material and the thickness of the polymer layer. To a

lesser extent, the time constant depends on sensor construction factors that affect the vapor penetration time through the porous electrode and on sensor ventilation (including the effect of removing or leaving the protective sensor cap). The time constant also depends on whether the ambient RH is increasing or decreasing (i.e., whether the sensor polymer is absorbing or desorbing water vapor). Time-lag error is discussed further in section 5.

3) BIAS ERRORS AND GROUND CHECK PROCEDURE

The occupation of binding sites in the sensor polymer by nonwater molecules causes a chemical contamination error. Experiments conducted at Vaisala show that the error is a dry bias whose magnitude depends on the measured temperature and RH, the sensor type (A vs H), age of the radiosonde, and storage temperature. A second dry-bias error is caused by long-term instability of the sensor polymer (sensor aging), which primarily depends on the age of the radiosonde. The total dry-bias error from both chemical contamination and sensor aging is composed of an offset portion and an RH-dependent portion. The offset portion of the dry-bias error can be corrected by using the ground check (GC) procedure, an option in the sounding software that allows an operator to enter an RH correction prior to launch based on the radiosonde measurement at 0% RH and the ambient temperature. The radiosonde's sensor arm is placed in a Vaisala-supplied container with desiccant that reduces the ambient RH to $<0.5\%$, and the measured RH is treated as a constant offset correction in the humidity model. The magnitude of the GC correction is typically 1%–3% RH. The total dry-bias error for the RS80-A under conditions of high RH is typically 3% RH for a radiosonde that is 6 months old and 5% RH for a radiosonde that is 1 yr old, increasing at a rate of 0.5%–1% RH per year thereafter. The contamination error by itself is less than 2% RH at high humidities below $-40°C$ for the RS80-A. The RS80-H is more susceptible to chemical contamination, with typical dry-bias errors of 5% RH at high humidities below $-40°C$, and maximum errors of 10% RH at high humidities at $+20°C$ for a radiosonde that is older than 1 yr.

Moist-bias error of a few percent RH due to sensor drift may occur under sustained conditions of high ambient RH. Moist-bias error may also result from condensation and icing on the sensor when exposed to supercooled liquid water or, to a much lesser extent, when exposed to ice-supersaturated conditions (Antikainen and Paukkunen 1994). Soundings affected by heavy icing are easily identified by noting that the RH measurement remains higher than a few percent RH well into the stratosphere. Vaisala has addressed the issue of sensor icing with their RS90-H radiosonde by using two humidity sensors that are alternately heated to remove condensation then allowed to recover before conducting the next measurement (Paukkunen 1995).

4) RANDOM UNCERTAINTIES

Random production uncertainty results from the combination of sensor-to-sensor production variability, small uncertainties in the general humidity model, and uncertainty in the calibration of the calibration chamber itself. The overall random production uncertainty is given by the manufacturer's specification for the accuracy of repeated calibrations, which is $\pm2\%$ RH at the 1σ or 68% confidence level (i.e., 68% of sensors have random uncertainty $<2\%$ RH) and $\pm4\%$ RH at the 2σ or 95% confidence level. Although the humidity model error and calibration chamber uncertainty are included in the above specification, they are systematic biases for a given sensor and may be either dry or moist by $<1\%$ RH below 75% RH and 1%–2% RH above 75% RH.

5) RADIATION CORRECTION

A radiation correction is applied to the temperature measurement in the data processing in order to address solar heating and infrared cooling of the temperature sensor, but no correction is made for radiative effects on the RH sensor. Uncertainty in the radiation correction for the temperature measurement indirectly introduces uncertainty into the RH measurement via the temperature dependence of the calibration. Radiation errors are included in the manufacturer's specification for the total random uncertainty in the tropospheric temperature measurement, about $\pm0.5°C$. The resulting uncertainty in RH due to the temperature dependence of the calibration is about $\pm0.3\%$ RH, which can safely be neglected. Solar radiation may directly affect the RH measurement if the RH sensor or the protective sensor cap warms the air at the surface of the sensor, decreasing the measured RH. The estimated maximum effect in the troposphere under clear-sky conditions is $<3\%$ to 4% RH at ice saturation and less at lower RH.

6) DEPENDENCE ON SENSOR TYPE

The corrections developed in this paper are only valid for the RS80-A sensor, not the RS80-H sensor. Both sensors are subject to the same general sources of measurement error, but the magnitude of each error differs substantially between the two sensor types. This difference is illustrated in Fig. 4, from simultaneous RS80-A and RS80-H measurements that passed through an orographic wave cloud. Simultaneous Formvar replicator measurements showed high concentrations of small, pristine ice crystals characteristic of wave clouds at temperatures below $-40°C$. Heymsfield and Miloshevich (1993, 1995) showed from in situ measurements and numerical modeling that the ambient RH in wave clouds with these microphysical characteristics will be very close to ice saturation, due to rapid depletion of excess water vapor by ice crystal growth. It is apparent from Fig. 4 that the nonlinear temperature-dependence
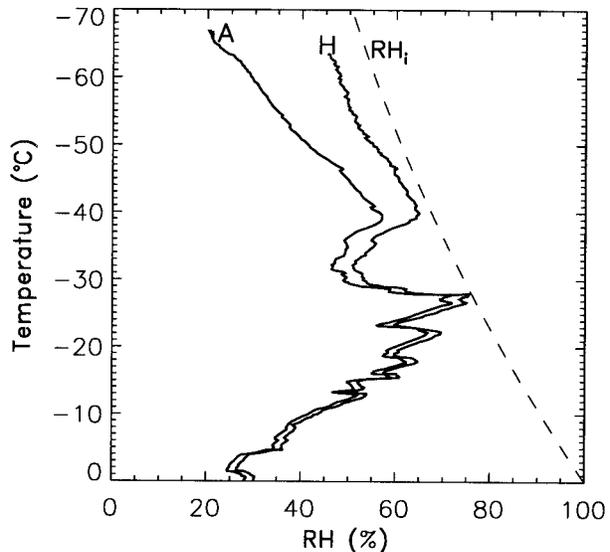

FIG. 4. Profiles of RH measured simultaneously by an RS80-A and an RS80-H radiosonde. Simultaneous Formvar replicator measurements showed that the radiosondes were in a deep orographic wave cloud at temperatures below $-40°C$. Dashed curve is ice saturation (RH$_i$).

algorithm used in the RS80-H data processing is considerably more accurate than the linear temperature-dependence algorithm used for the RS80-A. Laboratory measurements of the calibration of 20 RS80-H sensors were made by the National Institute of Standards and Technology (NIST) for Vaisala in 1990 (Antikainen and Paukkunen 1994; Semerjian 1990). The measurements showed an average measurement error of $\leq2\%$ RH in the temperature range $0°$ to $-40°C$ for humidities between 15% RH and ice saturation. At colder temperatures, laboratory measurements conducted at Vaisala showed that the RS80-H temperature-dependence error at ice saturation is 3% RH at $-50°C$ and 7% RH at $-60°C$, consistent with Fig. 4 and considerably less than the measurement error for the RS80-A at these temperatures.

c. The NOAA cryogenic frostpoint hygrometer

The design and measurement characteristics of the hygrometer are discussed by Vömel et al. (1995) and Oltmans and Hofmann (1995). The hygrometer measures water vapor concentration based on the chilled-mirror principle, where the temperature of a mirror is controlled to maintain a small and constant layer of frost coverage (below $0°C$). The mirror temperature under these conditions is equal to the frostpoint temperature of the air (T_f, the temperature at which the air would be saturated with respect to ice). The mirror is electrically heated or rapidly cooled by a cryogenic liquid that is $30°–90°C$ below T_f. Light from an LED is reflected by the mirror and detected by a phototransistor, which

is used by controller circuitry to maintain the constant layer of frost at T_f. The instrument is inherently capable of measuring ice supersaturation.

The mirror temperature is measured by a small bead thermistor just below the surface of the mirror and in excellent thermal contact with the mirror. The thermistors are individually calibrated between 0° and −79°C to an accuracy of ±0.05°C. The controller usually maintains the mirror temperature within a temperature range of ±0.3°C as it oscillates around T_f. Digitizing error is a maximum of 0.1°C at a temperature of 0°C, and self-heating of the thermistor is <0.1°C. Vömel et al. (1995) estimate the overall uncertainty in T_f to be better than ±0.5°C over the entire temperature range. The RH with respect to liquid water that is measured by the cryogenic hygrometer (RH$_c$) is calculated from T_f and from the air temperature (T) measured by an RS80-A radiosonde on the same instrument package, using the formula RH$_c$ = $e_i(T_f)/e_w(T)$ × 100%, where e_w is the saturation vapor pressure over liquid water as given by Wexler [1976; Eq. (15)], and e_i is the saturation vapor pressure over ice as given by Hyland and Wexler [1983; Eq. (18)].[2] The uncertainty in a derived RH$_c$ value depends on the uncertainty in both T_f and T, which is ±0.5°C for both measurements in the troposphere. The root-mean-square (rms) sum of the resulting random uncertainties, expressed as a fraction of RH$_c$, increases from 0.06 at 0°C to 0.10 at −70°C (i.e., ±6% to ±10% of the RH$_c$ value). Due to the temperature dependence of the ice-saturation curve, the uncertainty in RH$_c$ at ambient ice saturation is about 6% RH throughout the temperature range 0° to −70°C.

The gain of the controller circuitry is changed in-flight by a factor of 15–20 to compensate for the orders-of-magnitude difference in water vapor density between the troposphere and stratosphere, and to keep the frost layer constant over this range of conditions. Oscillations in the measurements sometimes occur shortly after launch until the controller stabilizes, but this behavior is obvious in the data (see the lowest portion of the hygrometer sounding in Fig. 1). Oscillations may also occur for short periods following the change in gain, but usually only during the ascent.

Since liquid water that condensed onto the mirror above 0°C can supercool if the mirror is clean and lacks ice nucleation sites, there is ambiguity over some temperature range as to whether the hygrometer is measuring the frostpoint or the dewpoint. In addition, soluble contaminants from dirty air near the surface may change the temperature of the condensate/vapor equilibrium from the normal frostpoint or dewpoint temperature. These artifacts are eliminated during the ascent by heating the mirror to 50°–100°C to remove conden-

sate and volatile contaminants, after which the frost layer forms directly from the gas phase, and ambiguity in the phase of the condensate is eliminated. The low-level clear is generally performed at 5–6-km altitude, above the freezing level.

The time response of the hygrometer has not been systematically studied. The time constant (63% response time) was measured for an earlier model of this hygrometer (Mastenbrook 1968) and found to be 21 s for an abrupt 3°C decrease in temperature at T_f = −85°C and 100-mb pressure, and 36 s at T_f = −90°C and 45-mb pressure. The instrument will respond faster as the frostpoint increases but slower as the air temperature increases, so its response time under tropospheric conditions is not well known. Figure 1 (at 10- and 13-km altitudes) shows that the hygrometer responds considerably faster than the RS80-A in the UT, but is a possible source of error when measurements from the hygrometer and RS80-A are compared.

4. Statistical correction approach

The dataset of simultaneous RS80-A and hygrometer measurements shown in Fig. 2 is used to derive a temperature-dependent correction for RS80-A measurements. This statistical approach will yield corrected RS80-A data that are, on average, equal to the corresponding hygrometer data at a given temperature. The uncertainty in corrected RS80-A data is evaluated in section 4b, and the sensitivity of the results to several properties of the dataset and assumptions in the analysis is discussed in section 4c.

a. Description of the dataset

The correction for RS80-A measurements is derived from statistical analysis of 95 RS80-A/hygrometer soundings taken near Boulder, Colorado. The RS80-A and hygrometer were launched on the same instrument package with a horizontal separation of about 70 cm and a sampling rate of 8 s. The soundings were typically conducted in the late morning once per month. Cloudy conditions were intentionally avoided, so sensor icing from supercooled liquid water does not impact the measurements. The hygrometer is designed to collect data on both the ascent and descent portions of the soundings, and the hygrometer data from the descent are generally superior to the data from the ascent because it is not affected by either the postlaunch oscillations in the controller circuitry or by outgassing from the balloon (outgassing is only an issue in the stratosphere, where water vapor concentrations and atmospheric pressure are very low). The balloon ascent and descent rates are both about 5 m s^{-1}, comparable to a standard radiosonde launch. It may be reasonable to also use the RS80-A descent data in this analysis because, unlike standard radiosonde soundings, the descent is controlled, so ventilation of the sensor is comparable to the ascent, and

---

[2] All results presented in this paper are affected by the choice for the formulation of the saturation vapor pressures, particularly at temperatures colder than −50°C. This issue is discussed in appendix B.
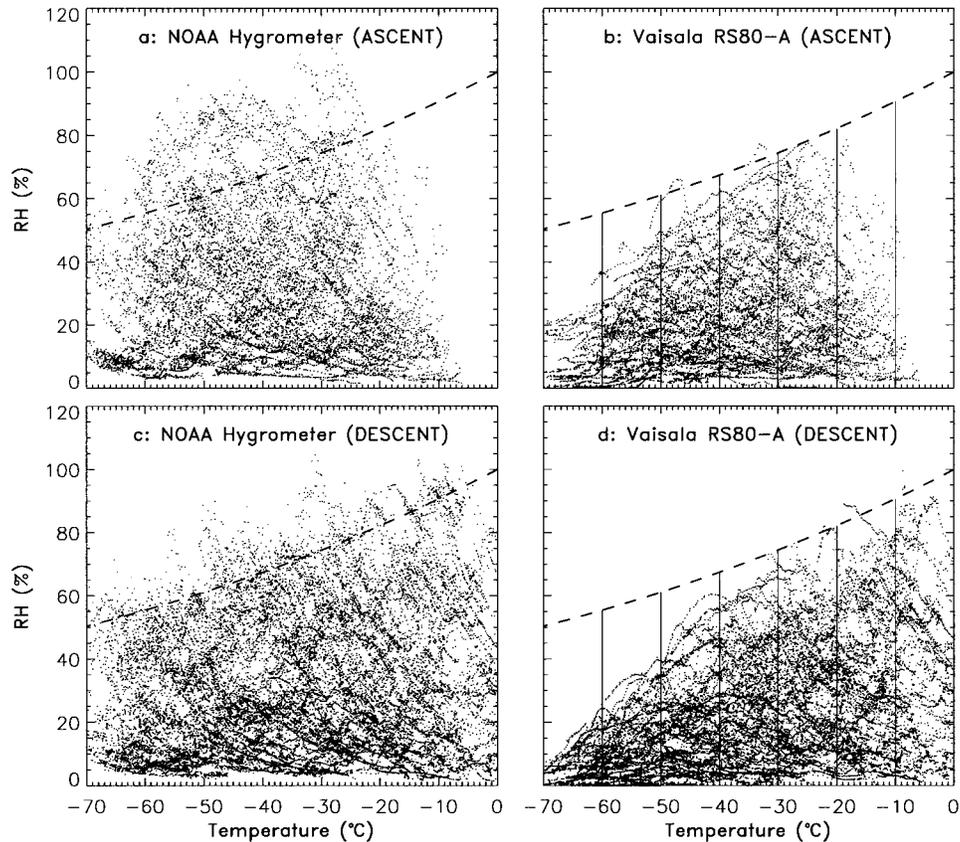
FIG. 5. The full dataset of simultaneous hygrometer measurements (left-hand panels) and corresponding RS80-A measurements (right-hand panels), separated into data from the ascent portion of the soundings (top panels) and data from the descent portion (bottom panels). The dataset used in the analysis and shown in Fig. 2 consists of the ascent data for temperatures colder than $-30°C$ and the descent data for temperatures warmer than $-30°C$. The vertical lines are for reference, and the dashed curves are ice saturation.

the upright orientation of the radiosonde is maintained on the instrument package. Any differences between the accuracy of the RS80-A ascent and descent data will be the consequence of either sampling the ambient profile in the reverse direction or changes in the sensor behavior after it has been exposed to the ambient conditions during the ascent.

A comparison of the RS80-A and hygrometer data from the ascent and descent portions of the soundings is shown in Fig. 5. The ascent data from the hygrometer at temperatures warmer than $-30°C$ are sparse in comparison to the descent data (Figs. 5a and 5c), in part because the postlaunch oscillations were eliminated from the dataset, and in part because ascent data below a 6-km altitude were eliminated since they precede the low-level clear. High-RH conditions at temperatures warmer than $-30°C$ are clearly underrepresented in the ascent data relative to low-RH conditions. Using these nonrepresentative ascent data at temperatures warmer than $-30°C$ to develop the correction is not statistically sound, partially because the RS80-A dry-bias errors

have a greater impact for low-RH conditions than for high-RH conditions. For example, a 5% RH bias error is a fractional error of 0.05 if the RH is 100%, but the fractional error is 0.25 if the RH is 20%. Therefore, the ascent data at temperatures warmer than $-30°C$ are unsuitable for statistical analysis as a result of hygrometer instrumentation artifacts. The descent data from the hygrometer are not affected by postlaunch oscillations or the low-level clear. Note that the maximum hygrometer RH values are slightly greater in the ascent data than in the descent data. This observation is consistent with a likely orographic effect, wherein the balloons ascend at the edge of the Rocky Mountains in air that in general is rising, cooling, and humidifying due to orography, whereas the descent is farther to the east in generally subsiding (drier) air over the Denver Basin.

The maximum RH values in the descent data from the RS80-A are lower than for the ascent data at temperatures colder than about $-40°C$, by an amount that increases with decreasing temperature (Figs. 5b and 5d). Clearly the RS80-A ascent and descent data are not

statistically equivalent for temperatures below $-40°C$, but the difference in maximum RH values disappears at temperatures above $-40°C$. Inspection of individual soundings and calculations of sensor response time presented in section 5c suggest that the sensors are slow to recover from typical stratospheric conditions near 0% RH, because the sensor response time is very slow at the cold temperatures in the UT. For example, if the ambient RH just below the tropopause at $-65°C$ is 40%, then the measured RH would increase from roughly 0% in the lower stratosphere to only 25% after one time constant (290 s at $-65°C$, or 1.5 km of descent). However, the time constant at $-40°C$ is only 27 s. The sensor will have fully recovered from the low stratospheric RH values before reaching the $-40°C$ temperature level and will no longer be influenced by the difference between starting a sounding under warm, moist conditions at the ground versus cold, dry conditions at the tropopause. At temperatures warmer than $-30°C$ (where the time constant is 13 s) there should be no significant difference in the measurements as a result of sampling the ambient RH profile in the reverse direction. The descent soundings also differ from the ascent soundings in that the sensor has already been exposed to the atmospheric conditions encountered during the ascent. Although exposure to the cold, dry conditions in the stratosphere will not alter sensor behavior, sustained conditions of high RH during the ascent may cause sensor drift of a few percent RH that will subsequently affect the descent measurements.

The following analysis is based on the combination of the ascent data at temperatures colder than $-30°C$ and the descent data at temperatures warmer than $-30°C$ (Fig. 2). The descent data are included in order to extend the temperature range of the correction from $-30°$ to $0°C$, and the above discussion is given as partial justification for considering the RS80-A descent data to be reliable at temperatures warmer than $-30°C$. Analysis presented later will show the sensitivity of the derived correction factor to the use of the descent data.

Sounding data from above the tropopause were excluded from the dataset based on an algorithm that searches for the base of the large-scale region having a lapse rate exceeding $-2°C$ km^{-1}. The resulting dataset contains few measurements at temperatures colder than $-69°C$, therefore the derived correction is valid for only tropospheric data in the temperature range $0°$ to about $-70°C$. Instances when the RS80-A measurement was $<1\%$ RH were also excluded from the dataset, because these values have undue influence on the correction factor, and the reporting precision of 0.1% RH is not meaningful.

b. Development of the statistical correction

The essence of the analysis is to derive a temperature-dependent correction function, $G(T)$, that when multiplied by a measured RS80-A value (RH_v) will yield a corrected value that on average is equal to the corresponding hygrometer measurement (RH_c) at a given temperature. That is, $G(T)$ satisfies the following condition:

$$\overline{\left[\frac{RH_v \times G(T)}{RH_c}\right]} = 1. \tag{1}$$

A practical approximation for $G(T)$ can be derived by considering a *constant* correction factor, G_i, for each 1°C temperature bin. The correction factor G_i is then determined from all data in the ith temperature bin:

$$G_i \times \overline{\left(\frac{RH_v}{RH_c}\right)} = 1. \tag{2}$$

The ratio of each corresponding measurement in the dataset, $RH_v/RH_c \equiv X$, is shown in Fig. 6a. Curves indicate the mean ($\overline{X}$) and standard deviation ($\overline{X} \pm \sigma_x$) in each 1°C temperature bin. The trend in $\overline{X}$ shows that on average the RS80-A measurements decrease with decreasing temperature to about 40% of the corresponding hygrometer measurements at $-70°C$. The RS80-A measurements slightly exceed the corresponding hygrometer measurements for temperatures warmer than $-10°C$.

The correction factors for each 1°C temperature bin, $G_i = 1/\overline{X}$, are shown in Fig. 6b. The desired correction function $G(T)$ is taken to be a polynomial fit through these points. A corrected RH_v measurement (RH'_v) is then given by

$$RH'_v = RH_v \times G(T), \tag{3}$$

where T is measured in degrees Celsius, and $G(T)$ is a fourth-order polynomial with the following coefficients: $a_0 = 0.9278$, $a_1 = -5.9662 \times 10^{-3}$, $a_2 = 1.5783 \times 10^{-4}$, $a_3 = 1.8179 \times 10^{-6}$, and $a_4 = 3.9407 \times 10^{-8}$. Note that $G(T)$ is only valid in the temperature range $0°$ to $-70°C$, and extrapolation beyond these limits is meaningless and gives extremely unreasonable results. Also note that, in addition to the temperature dependence given explicitly in $G(T)$, formulating the correction in terms of a multiplicative factor implicitly includes a linear dependence on RH since the corrected value RH'_v (and the amount of correction, $RH'_v - RH_v$) is linearly proportional to the measured value RH_v. This implicit linear RH dependence is reasonable because it is the same as the RH dependence of the dominant RS80-A measurement error (temperature-dependence error), as is shown in section 5a. The other RS80-A measurement errors (mainly time-lag and bias errors) have more complicated dependences that cannot be treated explicitly by this statistical approach, and it is primarily these errors that lead to the dispersion in the data at a given temperature that is seen in Fig. 6a.

The ratio of each corrected RS80-A measurement with the corresponding hygrometer measurement, $RH'_v/RH_c \equiv Y$, is shown in Fig. 6c. The fluctuations around
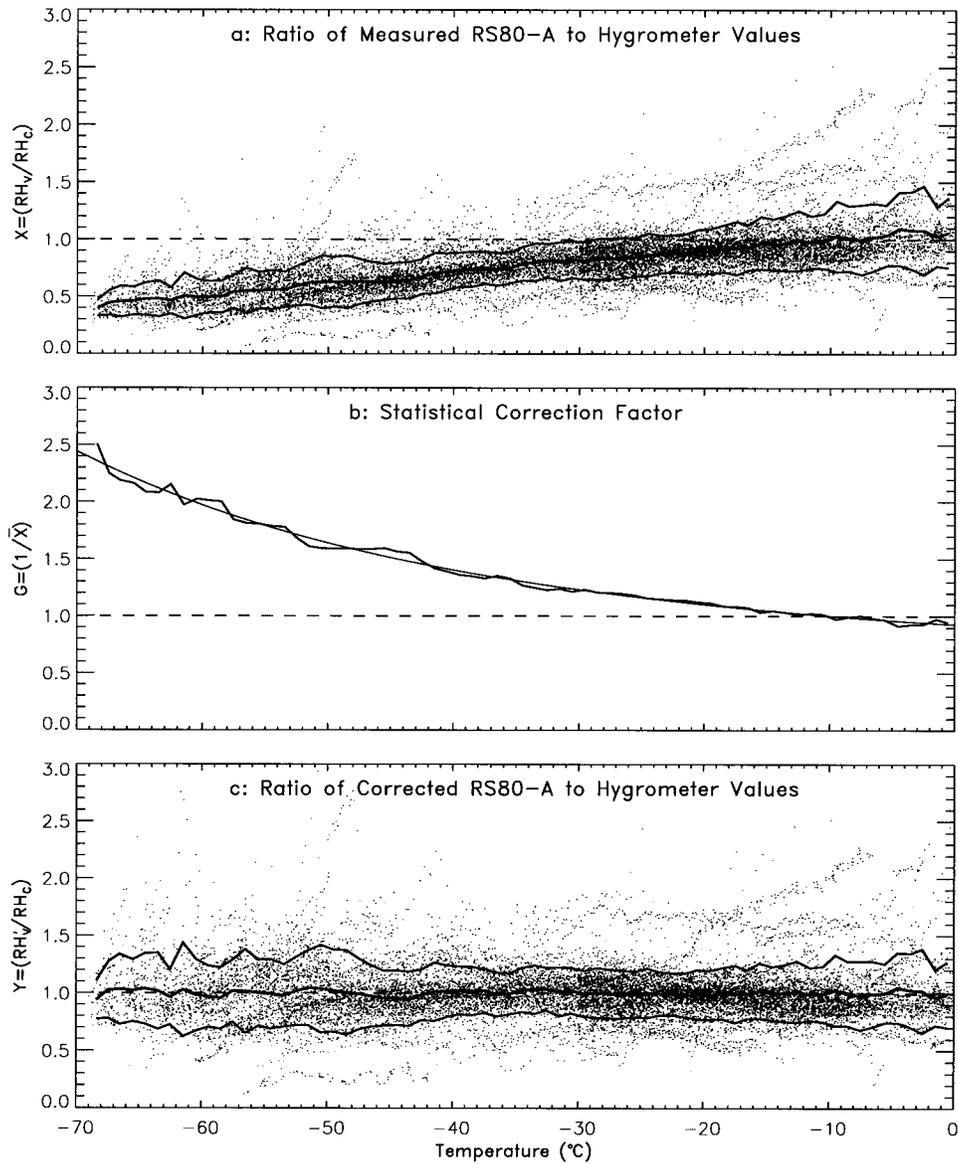
FIG. 6. (a) Ratio of each corresponding RS80-A and hygrometer measurement, with curves showing the mean ($\overline{X}$) and standard deviation ($\overline{X} \pm \sigma_x$) in each 1°C temperature bin. (b) The RS80-A correction factor for each 1°C temperature bin [G_i from Eq. (2)], and the polynomial fit to these values [$G(T)$ from Eq. (3)]. (c) Ratio of each corrected RS80-A measurement and the corresponding hygrometer measurement, with curves showing the mean ($\overline{Y}$) and standard deviation ($\overline{Y} \pm \sigma_y$) in each 1°C temperature bin.

$Y = 1.0$ of the mean ratio in each 1°C temperature bin are the consequence of curve-fit error that arises from using the curve fit $G(T)$ rather than the individual factors G_i to correct the data. The uncertainty in any given corrected measurement (Y_i) is characterized by the standard deviation of the measurements. Figure 7 shows the RS80-A dataset after correction using $G(T)$ from Eq. (3). Ice-supersaturated conditions are recovered even though the sensor is unable to measure these conditions, possibly because the ice supersaturation measured by the hygrometer is statistically represented in the dataset.

However, further analysis presented in section 5b suggests that these values are actually the consequence of a positive mean time-lag error.

c. Uncertainty assessment

The interpretation of uncertainty in the corrected data depends on whether one is statistically assessing a large dataset and is therefore concerned with uncertainty in the mean corrected values $\overline{Y}$, or whether one is correcting individual soundings and is therefore concerned
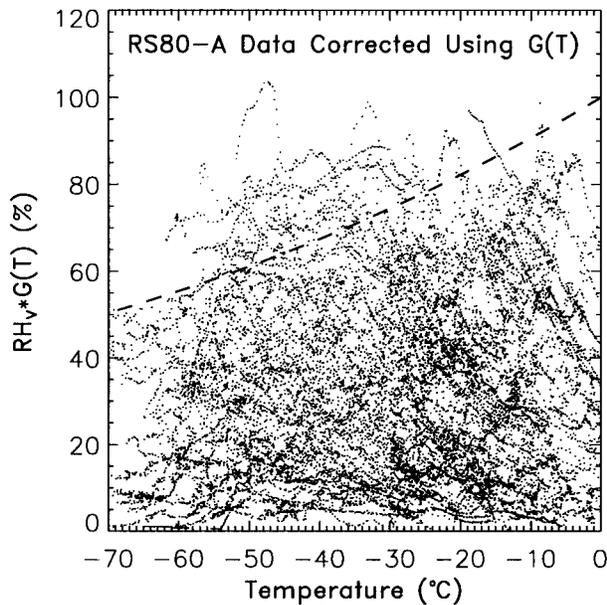
FIG. 7. The RS80-A dataset from Fig. 2b after correction using $G(T)$ from Eq. (3).

with uncertainty in a given corrected measurement Y_i. These two perspectives on uncertainty will be discussed separately.

The fractional uncertainty in the mean of corrected measurements at a given temperature, $\Delta\overline{Y}/\overline{Y}$, arises from the following sources and is summarized in Fig. 8a.

- The curve-fit error that results from using the curve fit $G(T)$ rather than the individual values $G_i(T)$ is a bias error at a given temperature of magnitude $G(T) - G_i(T)$. The fractional bias error in the mean of the corrected measurements is apparent from Fig. 6c and is easily shown to be $\Delta\overline{Y}/\overline{Y} = (\overline{Y} - 1)/\overline{Y}$ (curve labeled "B" in Fig. 8a).

- Random uncertainty in the individual G_i values (ΔG_i) results from statistical sampling uncertainty in the mean of the $\overline{X}$ measurements at a given temperature that are used to derive G_i. Sampling uncertainty in $\overline{X}$ is given by the standard deviation of the mean, $\sigma_{\overline{x}} = \sigma_x/\sqrt{N}$, where N is the number of data points in a given 1°C temperature bin. The upper and lower bounds describing the sampling uncertainty, $1/(\overline{X} \pm \sigma_{\overline{x}})$, correspond to the bounds describing the random uncertainty in the correction factor, $G_i \pm \Delta G_i$, and it can be shown that $\Delta G_i = \pm G_i^2 \sigma_{\overline{x}}$. Then the fractional random uncertainty in the mean corrected measurements $\overline{Y}$ is given by $\Delta\overline{Y}/\overline{Y} = \Delta G_i/G(T)$ (curve labeled "R" in Fig. 8a). It can be argued that the curve-fit bias error is just a manifestation of the underlying random sampling uncertainty in the dataset. The fluctuations in $G_i(T)$ around $G(T)$ in Fig. 6b may result from the sampling uncertainty in $\overline{X}$, and the curve-fit error would disappear with a greater sample size that better represents the (inherently smooth) underlying
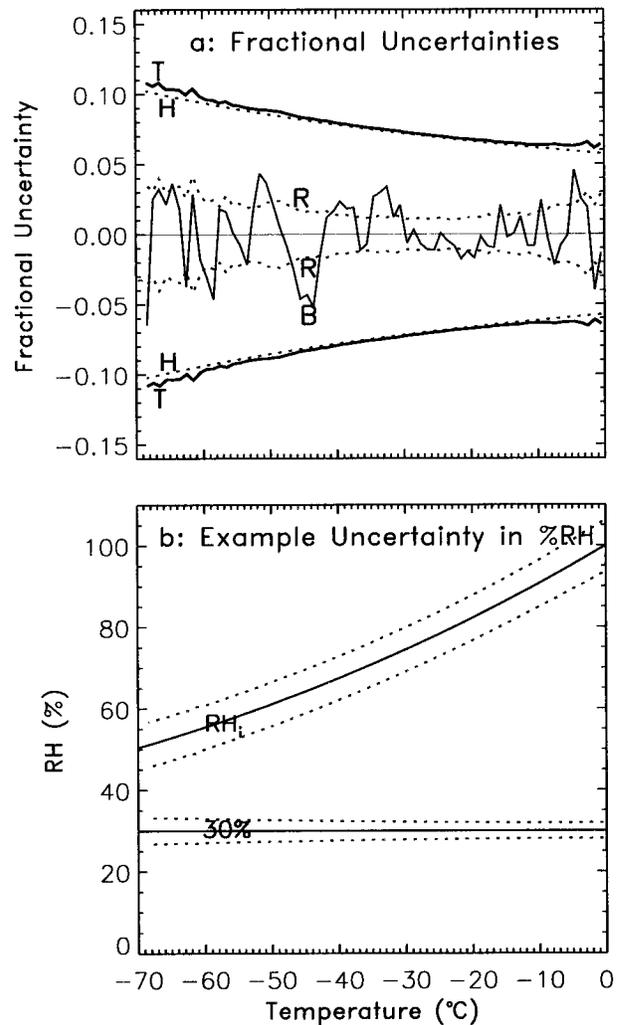

FIG. 8. (a) Summary of individual fractional uncertainties in the mean corrected RS80-A data ($\Delta\overline{Y}/\overline{Y}$). The total random uncertainty ($\pm$T) is composed of the statistical sampling uncertainty ($\pm$R) and the uncertainty in the hygrometer measurements ($\pm$H). The curve-fit bias error (B) is also shown. (b) Bounds of random uncertainty (dashed curves) if the mean corrected measurement is equal to either ice saturation or 30% RH (solid curves).

distribution. Support for this interpretation is seen in Fig. 8a in that the bias error ("B") and the random sampling uncertainty ("R") have a similar magnitude and temperature dependence.

- The overall fractional uncertainty in the corrected RS80-A data includes uncertainty in the hygrometer measurements, $\Delta RH_c/RH_c$. This uncertainty was calculated assuming random uncertainties of $\pm$0.5°C in both the frostpoint and air temperature measurements. The uncertainty in the hygrometer measurements is the rms sum of the frostpoint and air temperature contributions (curve labeled "H" in Fig. 8a).

The random uncertainties contributed by the sampling statistics and the hygrometer are independent, and their

rms sum is the total random uncertainty in the mean corrected RS80-A measurements (curve labeled "T" in Fig. 8a). The fractional uncertainty increases with decreasing temperature from about 0.06 at 0°C to 0.11 at −70°C and is dominated by uncertainty in the hygrometer measurements. This uncertainty will henceforth be considered the total uncertainty in the mean corrected RS80-A measurements, with the interpretation that the curve-fit bias error duplicates and, in some sense, characterizes the random sampling error ΔG_i. As a sample application, Fig. 8b shows the uncertainty, in terms of RH percentage, if the mean corrected measurement is equal to either ice saturation or to 30% RH.

The uncertainty assessment given thus far has concerned uncertainty in the mean of corrected data as a function of temperature when $G(T)$ is applied statistically to large datasets. However, considerably greater uncertainty for any individual measurement is indicated by the large dispersion of the measurements around the mean (Fig. 6c), which is a consequence of time-lag, bias, and other errors that are not solely temperature dependent. The correction accounts for only the average value of time-lag and bias errors at a given temperature, so the effect of these profile-specific and sensor-specific errors on any given measurement is not accounted for by this temperature-dependent correction approach. The uncertainty for any given corrected measurement can be quantified in terms of the dispersion of the corrected measurements around the mean.

Figure 9a shows the 68th and 95th percentiles of the corrected data above and below the mean from Fig. 6c, where these percentiles are analogous to the 1σ and 2σ confidence levels for Gaussian distributions. The curves have been smoothed by averaging each 1°C point with its two neighbors, to aid interpretation but without significant loss of information. Any given corrected measurement has a 68% probability of lying between P_{68}^{+} and P_{68}^{-}, where "+" and "−" indicate above and below the mean, respectively. The 68% confidence interval is roughly symmetric about the mean, but the 95% interval is skewed over part of the temperature range by the outlying values seen in Fig. 6a. The fractional uncertainty for any given corrected measurement at the 68% confidence level is near ±0.2 (or 20% of the RH value) over most of the temperature range, but the uncertainty is generally greater than ±0.4 at the 95% confidence level. The uncertainty in a given corrected measurement at the 68% confidence level is considerably greater than the uncertainty in the mean of corrected measurements (±0.06 to ±0.11 at the 1σ confidence level). Figure 9b shows the uncertainty in RH percentage at the 68% confidence level for an individual corrected measurement that is either at ice saturation or at 30% RH. The uncertainty at the 95% confidence level is about twice that shown in Fig. 9b over most of the temperature range.

Several factors may effect the generality of $G(T)$ and its uncertainty when other datasets are considered.
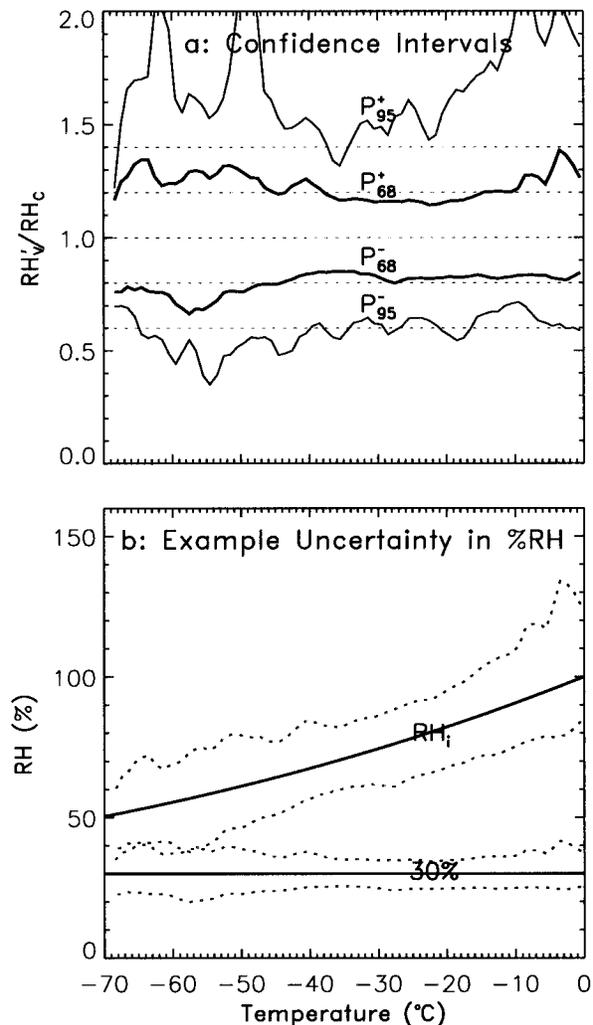

FIG. 9. (a) Confidence intervals encompassing 68% ($P_{68}^{\pm}$) and 95% ($P_{95}^{\pm}$) of the corrected RS80-A measurements, relative to the mean at $Y = 1.0$. (b) The 68% confidence interval for an individual corrected measurement that is at either ice saturation or 30% RH.

Time-lag errors depend on the temperature profile and the instantaneous rate of change of ambient RH during a sounding, and therefore $G(T)$ contains the mean time-lag error as a function of temperature for profiles that are typical of Boulder, a particular midlatitude continental location. If a different location is characterized by substantially different temperature and humidity profiles (e.g., a maritime, tropical location), then the mean time-lag errors in such a dataset may be different from those at Boulder. There is not a second hygrometer dataset of sufficient size from another location to reasonably assess a possible dependence on geographic location; however, the impact of all profile-specific and sensor-specific measurement errors on $G(T)$ is derived in section 5b. A second generality issue is that the radiosonde ground check correction was not performed in making these measurements, and therefore $G(T)$ cor-
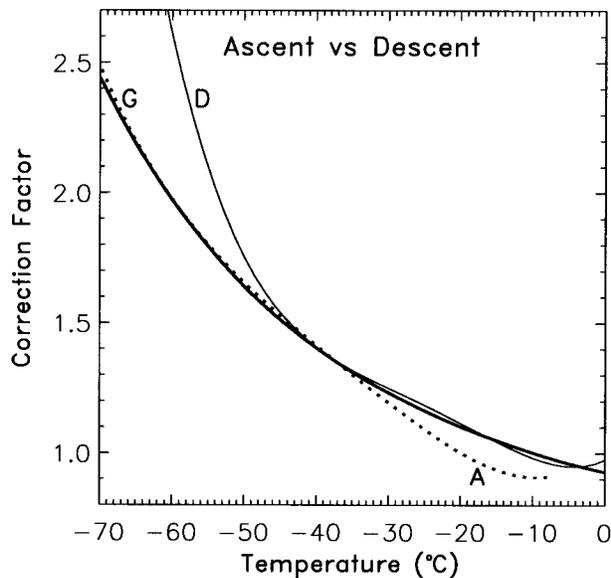
FIG. 10. Effect on $G(T)$ of combining the ascent and descent data. Curves show the correction factor as calculated from only the ascent data over the full temperature range (dashed curve, "A"), from only the descent data over the full temperature range (solid, "D"), and from the combined dataset used to derive $G(T)$ (bold, "G"). The small fluctuations and endpoint behavior of the curves are artificial consequences of the polynomial curve fits.
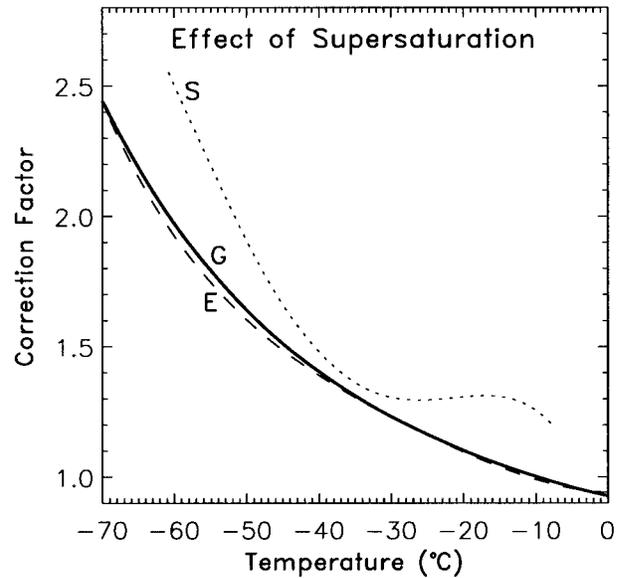

FIG. 11. Effect on $G(T)$ of ambient ice supersaturation. Curves show the correction factor as calculated from the standard dataset used to derive $G(T)$ (bold curve, "G"), from the dataset excluding instances when RH_c exceeds ice saturation (dashed, "E"), and from *only* the instances when RH_c exceeds ice saturation (dotted, "S").

rects for mean bias errors that may already have been partially corrected in other datasets if the GC correction was performed. Finally, all results presented in this paper are affected at temperatures below $-40°C$ by the choice for the formulation of the saturation vapor pressures, as discussed in appendix B.

d. Sensitivity investigations

Figure 10 shows the impact on $G(T)$ of combining the ascent data for temperatures colder than $-30°C$ with the descent data for temperatures warmer than $-30°C$. The correction has been derived using only the ascent data over the full temperature range (labeled "A"), or only the descent data over the full temperature range ("D"), or using the combined dataset that was used to derive $G(T)$ ("G"). The large correction factor for the descent data at temperatures below $-50°C$ is attributed to the slow sensor time response at very cold temperatures and consequent slow recovery from low stratospheric humidities. The sensor responds faster as the temperature increases, and the ascent and descent curves are essentially equal between $-45°$ and $-30°C$. At temperatures warmer than $-30°C$ the difference between the curves slightly exceeds the uncertainty in $G(T)$. The ascent data at temperatures above $-30°C$ were deemed unreliable as a result of hygrometer instrumentation artifacts that follow the launch. A case was made that the RS80-A descent data are reliable for temperatures warmer than $-30°C$ because the descent is controlled,

and sensor ventilation and orientation are similar to the ascent. This case is supported by the similarity of the ascent and descent curves between $-30°$ and $-45°C$, where the ascent data are reliable. Unknown differences between the ascent and descent measurements will at worst affect only the temperature range $0°$ to $-30°C$, where the correction factor is relatively small.

The RS80-A will sense ice-saturated air whenever the ambient air is ice supersaturated. Figure 11 shows the contribution to $G(T)$ of ice-supersaturated ambient conditions in the dataset. The correction factor that is derived from only the data when the hygrometer measured ice supersaturation (labeled "S") is substantially greater than $G(T)$, indicating that the measurement error for ice-supersaturated conditions is greater than the mean measurement error for the dataset as a whole. However, the correction factor derived by excluding only the ice-supersaturated conditions from the dataset ("E") differs very little from $G(T)$, showing that the presence or absence of ice-supersaturated conditions does not substantially affect the analysis, because the frequency of ice-supersaturated conditions in the dataset is relatively minor.

Figure 12 investigates the possibility of an RH dependence in the dataset that is beyond the linear RH dependence implicit in both $G(T)$ and the temperature-dependence error. Four correction curves were each derived by partitioning the RS80-A data into one of four equal RH intervals between 0% RH and ice saturation. The corrections for all four RH intervals are very similar and do not display any systematic trend that would indicate an additional RH dependence.
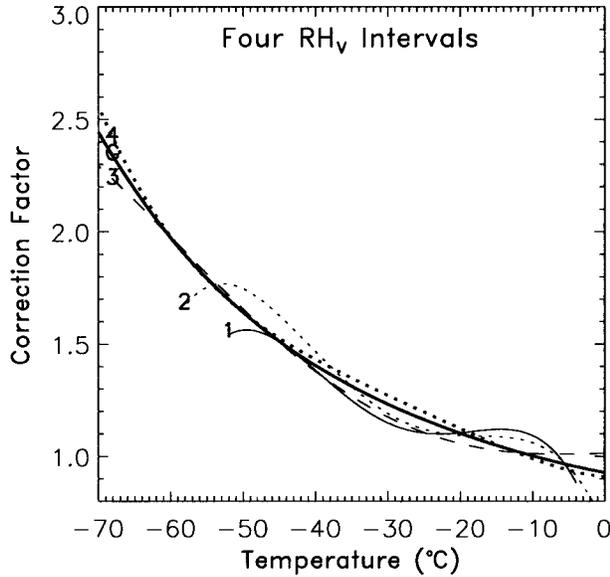
FIG. 12. Dependence of $G(T)$ on RH. Numbered curves show four correction factors each derived by selecting the RS80-A data from one of four equally spaced RH intervals between 0% RH and ice saturation (RH_i). The curve labeled "1" is the correction factor for RS80-A data in the interval $RH_v = 0.75$–$1.0 \times RH_i$, and the curve labeled "4" is the correction factor for RS80-A data in the interval $RH_v = 0.0$–$0.25 \times RH_i$. The bold curve ("G") is $G(T)$. The behavior near the end points of curves "1" and "2" results from a small sample size.

5. Individual RS80-A measurement errors

This section investigates several of the individual RS80-A measurement errors in greater detail than was given in section 3b, which will provide further insight into the statistical correction. The framework for a second correction approach is also developed, based on understanding and correcting the individual RS80-A measurement errors.

a. Correction for temperature-dependence error

Calibration chamber measurements were conducted by Vaisala to derive a correction for the temperature-dependence error that results from using a linear approximation in the data processing to represent the nonlinear temperature dependence of the sensor calibration. The RH dependence of the sensors is given by the general humidity model, modified according to the individual sensor calibration at $+20°C$. The temperature dependence of the sensors is given by two linear curves that approximate the temperature dependence at 0% RH and at saturation (ice saturation below 0°C or 100% RH above 0°C). The linear approximation at 0% RH is very accurate; however, the linear approximation at ice saturation (RH_i) is increasingly inaccurate at decreasing temperatures. The data processing algorithm calculates the reported measurement, RH_v, by scaling the humidity model between the (accurate) temperature-dependence curve at 0% RH and the (inaccurate) temperature-dependence curve at RH_i. A correction for the temperature-dependence error in processed data, where the linear approximation at RH_i has already been applied, is given by rescaling the measurement by the ratio $RH_i/RH_{v,i}$, where $RH_{v,i}$ is the RH reported by the data processing algorithm when the ambient RH is known to be at RH_i. This simple linear rescaling of the measured values is appropriate because the nonlinear RH dependence of the calibration has already been accounted for in the normal data processing, and the error simply results from scaling the RH dependence between the (accurate) temperature-dependence curve at 0% RH and the (inaccurate) temperature-dependence curve that yields the value $RH_{v,i}$ instead of RH_i.

Accurate measurements of $RH_{v,i}$ were made in a calibration chamber at Vaisala using 16 sensors that were each enclosed in a sealed "ice cap." The calibration chamber was cooled and the sensors allowed to reach a steady state at each measurement temperature in such a way that excess water vapor condensed onto the interior of the cap and not directly on the sensor. Therefore, the ice on the interior of the cap maintained the air that was in contact with the sensor at RH_i, and the data processing algorithm reported $RH_{v,i}$. The sampled air within the ice cap is inferred from fundamental physical principles to be at the natural steady-state saturation humidity (i.e., the "true" value of ice saturation, independent of any choice for the formulation of saturation vapor pressure and of any humidity reference in the calibration chamber). The temperature measurements were taken from the radiosonde temperature sensor (also within the ice cap), so this experiment does not depend on any external temperature or humidity references. Measurements were made at ice saturation for temperatures down to $-65°C$. Additional measurements were made over the full humidity range from 0% to 100% RH at the standard calibration temperature of $+20°C$, in order to correct each sensor's measurements for small random uncertainties in the general humidity model. The difference between the measured $RH_{v,i}$ and the ambient RH_i was due only to the temperature-dependence error, since the humidity model errors were removed and the experiment was conducted in a steady state so that sensor time response was not a factor. Figure 13a shows the measured $RH_{v,i}$ values at each measurement temperature (dashed curve). The required amount of correction is $RH_i - RH_{v,i}$, which is represented as a continuous function of temperature by the polynomial fit $C(T)$ (solid curve). Figure 13b shows the resulting correction factor for temperature-dependence error, $RH_i/RH_{v,i} \equiv F(T)$. A corrected RH_v measurement is given by $RH_v' = RH_v \times F(T)$. The form of $F(T)$ is not amenable to an accurate polynomial fit, but can be expressed in terms of $C(T)$:

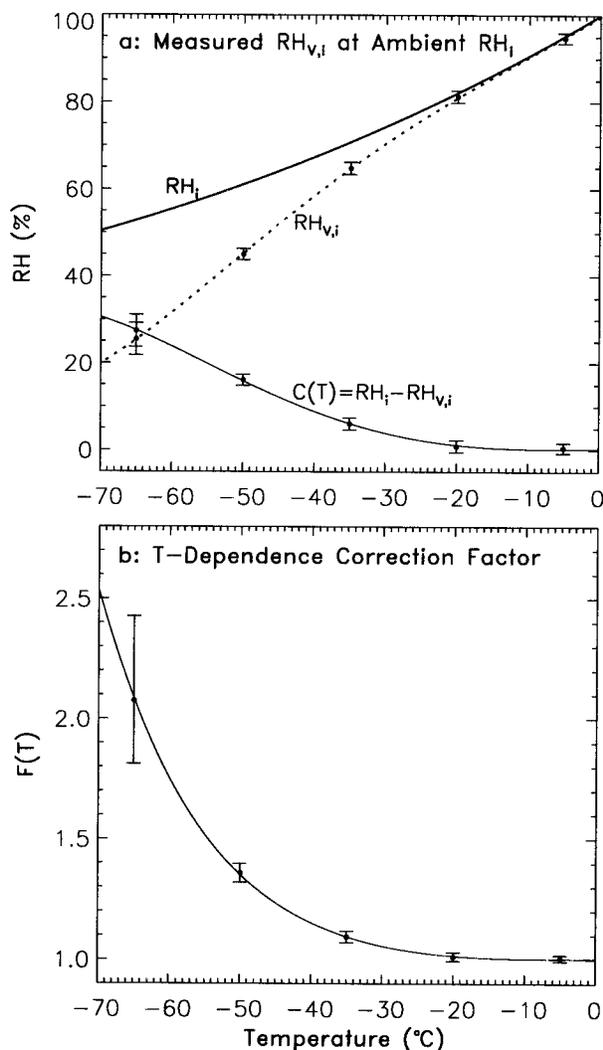$$F(T) = \frac{RH_i(T)}{RH_i(T) - C(T)}, \qquad (4)$$

FIG. 14. The RS80-A dataset from Fig. 2b after correction for temperature-dependence error using $F(T)$ from Eq. (4).

FIG. 13. (a) Mean and standard deviation of the measured RH values ($RH_{v,i}$) for known ambient conditions of ice saturation (RH_i), from the ice-cap experiment. The temperature-dependence error at ambient RH_i is equal to $RH_i - RH_{v,i}$, and $C(T)$ is a polynomial fit to these points. (b) Correction factor for RS80-A temperature-dependence error, given by $F(T)$ in Eq. (4). Error bars on $F(T)$ correspond to the standard deviation bars on $C(T)$.

where T is measured in degrees Celsius, $RH_i(T) = e_i(T)/e_w(T) \times 100\%$ as calculated from the Wexler/Hyland formulations for the saturation vapor pressures described in appendix B, and $C(T)$ is a fifth-order polynomial with the following coefficients: $a_0 = 0.3475$, $a_1 = 2.83 \times 10^{-2}$, $a_2 = 4.209 \times 10^{-4}$, $a_3 = -1.4894 \times 10^{-4}$, $a_4 = 6.4325 \times 10^{-7}$, and $a_5 = 2.1677 \times 10^{-8}$. Additional data points warmer than $+20°C$ and colder than $-65°C$ were also specified in deriving $C(T)$, to make extrapolation sensible and accurate over a wide temperature range, based on knowledge of the behavior of the sensors at those temperatures.

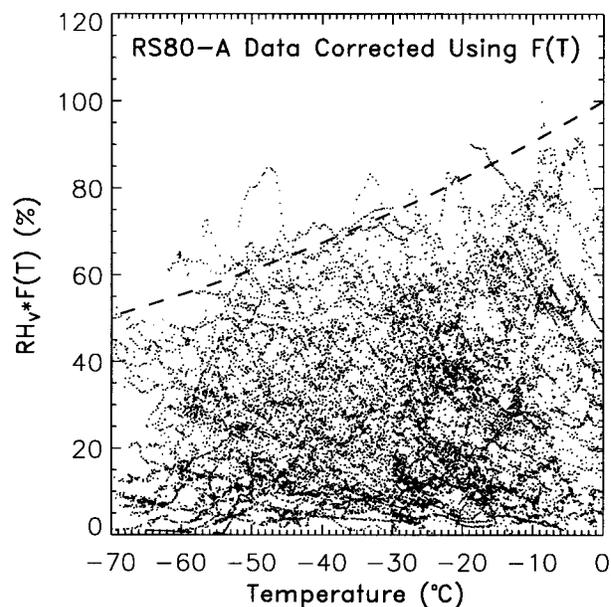The correction factor for temperature-dependence error, $F(T)$, is near 1.0 at temperatures warmer than $-25°C$, indicating that the linear approximation in the data processing algorithm is accurate at these temperatures. Below about $-30°C$, $F(T)$ increases substantially with decreasing temperature. When the RS80-A dataset from Fig. 2b is corrected for temperature-dependence error (Fig. 14), the maximum corrected RH values are approximately equal to ice saturation, as should be true for the moistest ambient conditions in the dataset. Note that $F(T)$ is based on the linear temperature-dependence approximation currently in use, which last changed in October 1985.

b. Mean time-lag and bias errors

When the RS80-A dataset is corrected for temperature-dependence error, the residual measurement errors in the dataset are primarily time-lag and bias errors. A correction for the mean of these residual errors as a function of temperature, $G'(T)$, can be derived from the RS80-A/hygrometer dataset by the same approach used in section 4, but after each measurement (RH_v) is first corrected for temperature-dependence error. The ratio of each corrected RS80-A measurement [$RH_v \times F(T)$] to the corresponding hygrometer measurement (RH_c) is shown in Fig. 15a, analogous to Fig. 6a. The correction factor $G'(T)$ for the mean of the residual errors is given as before by a polynomial fit to the reciprocal of this ratio in $1°C$ temperature bins (Fig. 15b, labeled "G'"). A corrected RS80-A measurement (RH'_v) is then given by first correcting for temperature-dependence error and then correcting for the mean of the residual measurement errors:

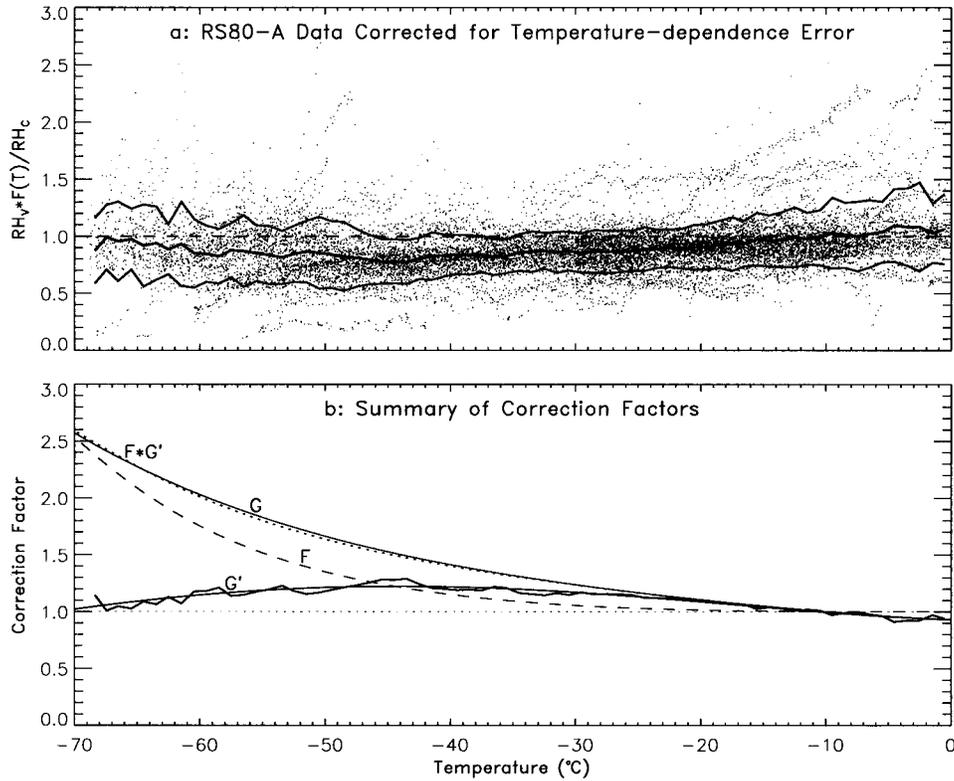$$RH'_v = RH_v \times F(T) \times G'(T), \qquad (5)$$

FIG. 15. (a) Ratio of corresponding RS80-A and hygrometer measurements as described in Fig. 6a, but after correcting the RS80-A measurements for temperature-dependence error. Curves show the mean and standard deviation in each 1°C temperature bin. (b) The correction factor for the residual measurement errors in each 1°C temperature bin (bold), where the polynomial fit to these points is $G'(T)$ from Eq. (5). The other correction factors are shown for comparison: the statistical correction factor for all measurement errors combined, $G(T)$ from Eq. (3) (solid); the correction factor for temperature-dependence error, $F(T)$ from Eq. (4) (long dashes); and the alternative correction factor for all measurement errors, the product $F(T) \times G'(T)$ (short dashes).

where T is measured in degrees Celsius, and $G'(T)$ is a fourth-order polynomial with the following coefficients: $a_0 = 0.93095$, $a_1 = -3.7498 \times 10^{-3}$, $a_2 = 3.5334 \times 10^{-4}$, $a_3 = 8.2217 \times 10^{-6}$, and $a_4 = 3.8184 \times 10^{-8}$.

Both correction approaches—$G(T)$ versus $F(T) \times G'(T)$—are based on the same information, and they are shown in Fig. 15b to be essentially equal within the limitation that all three functions are polynomial fits that contain curve-fit error. Figure 15b shows that on average the temperature-dependence error is the dominant contribution to the total measurement error at temperatures below about −45°C, whereas other errors dominate (on average) at warmer temperatures. If $G'(T)$ is interpreted as mainly representing time-lag and bias errors, then on average these sources of error result in a dry bias over most of the temperature range [because $G'(T) > 1.0$]. The measurement errors that contribute to $G'(T)$ can potentially vary for different locations or different datasets, whereas the temperature-dependence error and $F(T)$ do not vary for different locations or datasets.

Both correction approaches—$G(T)$ versus $F(T) \times$

$G'(T)$—have the same relatively large uncertainties when used to correct an individual sounding, as a result of the profile-specific and sensor-specific errors. Alternatively, one can correct individual soundings for only the temperature-dependence error, then inspect the result and judge the impact of the bias and time-lag errors based on knowledge of their dependences and approximate magnitudes. Improved accuracy for correcting individual soundings will be possible when ongoing work by several groups on correcting bias and time-lag errors is completed.

c. Effects of time response

Operational RH measurements do not occur under the steady-state conditions that characterize the sensor calibration procedure or the ice-cap experiment. The time constant (63% response time) for the Vaisala RH sensors depends primarily on temperature and to a lesser extent on whether the RH is increasing or decreasing. It is therefore possible to correct the RH measurements for time-lag error using the radiosonde temperature mea-

surements if the temperature dependence of the time constant is known. The time constant (τ) of the RS80-A sensor was measured as a function of temperature by NIST for Vaisala in 1981. The NIST measurements will be used in detail in a future study on correcting time-lag error; however, for the present purpose of characterizing time-lag effects, Vaisala has determined from the NIST data the following approximation for the average temperature dependence of the RS80-A time constant:

$$\tau(T) \approx 10^{(0.23045-0.03004T)}, \tag{6}$$

where τ is measured in seconds and T in degrees Celsius. The time constant increases with decreasing temperature from 7 s at $-20°C$ to 27 s at $-40°C$, 108 s at $-60°C$, and 215 s at $-70°C$. These time-constant values are consistent with earlier measurements reported by Salasmaa and Kostamo (1975). The sensor responds as a typical exponential function of time, so the 90% response time is a factor of 2.3 longer than the 63% response time. The RS80-H responds somewhat more slowly than the RS80-A.

The rate of change of the measured RH at any given instant is proportional to the time constant and to the difference at that instant between the measured RH and the ambient RH. Therefore the time-lag error at any instant depends on how rapidly the ambient RH is increasing or decreasing, and also depends on the ambient RH and temperature profiles at earlier times through their cumulative effect on the measured RH at a given instant. Sample time-lag errors are calculated here for the purpose of assessing their approximate magnitudes and impact on operational data. If the ambient RH (RH_a) is treated as a series of step changes and the temperature (T) is constant at each step, then the measured RH (RH_v) as a function of time relative to its value when the step change occurs at time $t = 0$ (RH_0) is readily shown to be

$$RH_v(t, T) \approx RH_a - (RH_a - RH_0)\, e^{-t/\tau(T)}. \tag{7}$$

Figure 16 shows simulated RS80-A measurements for specified profiles of RH_a and T, based on Eqs. (6) and (7). The simulated profile is a cloud layer at ice saturation of thickness 2 km between dry layers at $RH_a = 10\%$, where RH_a above and below the cloud varies linearly over a distance of 0.5 km. The simulations assumed step changes in RH_a and T every 1 s, an ascent rate of 5 m s^{-1}, and a lapse rate of $-6.5°C$ km^{-1}. Three different initial temperatures at the base of the simulation (T_0) are shown. The simulated measurements in the left-hand panels show that time-lag error causes a smoothing of the ambient RH profile by an amount that increases with decreasing temperature. The effect of temperature is also seen by noting that the region of decreasing RH_a above cloud top in each profile has the same slope as the region of increasing RH_a below the cloud, but is about 15°C colder. The corresponding right-hand panels show the magnitude of the time-lag
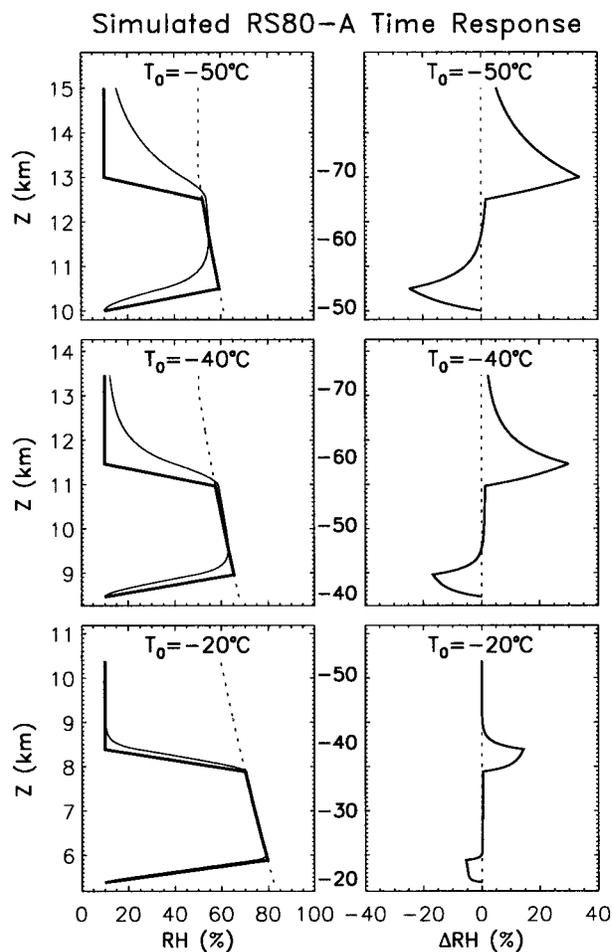

FIG. 16. (left) Simulations of RH that would be measured by the RS80-A (light curves) for the ambient temperature and RH profiles described in the text (bold curves) and for three different initial temperatures at the base of each simulation (T_0). The altitude scale is derived from a temperature of 15°C at $Z = 0$ and a lapse rate of $-6.5°C$ km^{-1} (the temperature is held constant at $-70°C$ above $Z = 13$ km to simulate the tropopause). (right) The time-lag error corresponding to the left-hand panels, given by the difference between the measured and ambient RH. Temperatures (°C) are indicated between the panels.

error (i.e., $\Delta RH = RH_v - RH_a$) and its strong dependence on temperature. The ambient conditions simulated in the center panels ($T_0 = -40°C$) are similar to the ambient conditions for the sounding shown in Fig. 1, and the observed and simulated time-lag effects are similar. The simulated RH profiles are realistic, though toward the extreme end of typical atmospheric rates of change in RH, and therefore the simulations give a reasonable idea of maximum time-lag errors that are likely present in the RS80-A dataset and in operational RS80-A measurements. These near-maximum time-lag errors vary with temperature from about $\pm5\%$ RH at $-20°C$ to $\pm15\%$ RH at $-40°C$, $\pm25\%$ RH at $-50°C$, $\pm30\%$ RH at $-60°C$, and $\pm35\%$ RH at $-70°C$. Typical time-lag errors are considerably less but will vary wide-

ly depending on the specific ambient RH profile. It is obvious that the ability to resolve fine structure in the ambient RH profile decreases with decreasing temperature.

These simulations illustrate the large magnitudes and range of variability that are possible for time-lag errors, which supports the assertion that they play a dominant role in producing the large dispersion in the measurements and the consequent large uncertainty when $G(T)$ or $G'(T)$ is applied to an individual sounding. The temperature dependence of $G'(T)$ largely reflects statistical characteristics of the ambient temperature and humidity profiles and the resulting mean time-lag errors.

6. Application of the corrections

The corrections are applied to two RS80-A soundings and compared to simultaneous hygrometer measurements in Fig. 17. These soundings contain measurements in both dry air and in cirrus clouds, and Fig. 17a is the same sounding as in Fig. 1.

Corrected RS80-A measurements should ideally be very close to ice saturation in the upper portion of the regions where the hygrometer measured ice supersaturation, because time-lag error should be minimal after sustained exposure to ice-supersaturated air (see Fig. 16). Measurements corrected using $G(T)$ are near or above ice saturation when the hygrometer measures ice supersaturation. Measurements corrected for only the temperature-dependence error are 5%–10% RH below ice saturation in these regions, which is consistent with dry-bias errors of a few percent RH and random production uncertainty of a few percent RH.

The amount of difference between the profiles corrected with $F(T)$ and with $G(T)$ reflects the contribution of the mean time-lag and bias errors. In the lower portion of the sounding in Fig. 17b, $G(T)$ yields corrected measurements that are higher than the hygrometer measurements, whereas in Fig. 17a the corrected measurements in this temperature range are slightly lower than the hygrometer measurements, illustrating that the mean time-lag and bias errors contained in $G(T)$ differ from the actual errors for a particular sounding.

An overall conclusion from Fig. 17 is that correction of the measurements using either $G(T)$ or $F(T)$ substantially improves the measurements for almost all atmospheric conditions, particularly at cold temperatures. The one exception might be at temperatures colder than $-60°$ or $-65°C$, where the time response is so slow that changes in the ambient RH are only detected after a very long time, underscoring the need for a detailed time-lag correction.

7. Conclusions

This study has characterized relative humidity measurements from Vaisala RS80-A radiosondes at temperatures between $0°$ and $-70°C$. Sources of measure-
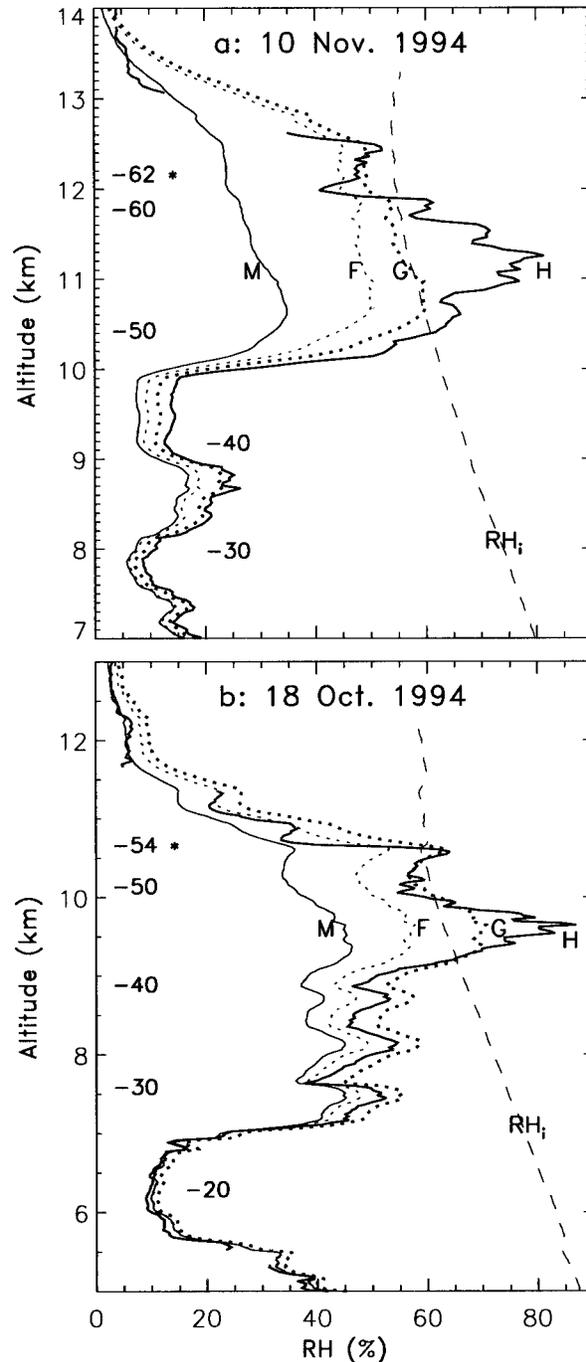

FIG. 17. Example of corrections applied to two RS80-A soundings. Shown are RH_c measured by the hygrometer ("H"), RH_v measured by the RS80-A ("M"), RH_v corrected using $G(T)$ from Eq. (3) ("G"), RH_v corrected for only temperature-dependence error using $F(T)$ from Eq. (4) ("F"), and ice saturation (RH_i). The tropopause is indicated with an asterisk, and temperatures (°C) are indicated at various altitudes.

ment error were identified and two approaches for correcting the errors were presented. The corrections given in this paper must be applied only to Vaisala RS80-A measurements. The RS80-H and RS90-H sensors are subject to the same general sources of measurement error, but the magnitude of each error depends strongly on the sensor type.

A temperature-dependent correction factor was derived from statistical analysis of simultaneous measurements from RS80-A radiosondes and the NOAA cryogenic frostpoint hygrometer. This correction factor, $G(T)$ from Eq. (3), corrects for the mean of all measurement errors as a function of temperature, and its magnitude is about 1.3 at $-35°C$, 1.6 at $-50°C$, 2.0 at $-60°C$, and 2.4 at $-70°C$. The fractional uncertainty in the mean of the corrected data at a given temperature, when $G(T)$ is applied statistically to large datasets, is between $±0.06$ at $0°C$ and $±0.11$ at $-70°C$ (i.e., 6%–11% of the corrected RH values) at the 1σ confidence level. The fractional uncertainty for any individual corrected measurement, when $G(T)$ is applied to an individual sounding, is about $±0.2$ at the 68% confidence level and $±0.4$ at the 95% confidence level. The greater magnitude of the latter uncertainty indicates that $G(T)$ more accurately corrects large datasets than individual soundings. $G(T)$ should not be used outside the temperature range $0°$ to $-70°C$ because it is a polynomial fit, and its extrapolation is meaningless and gives enormous errors.

The RS80-A is subject to several types of measurement errors. Temperature-dependence error results from using a linear approximation in the data processing to represent the actual nonlinear temperature dependence of the sensor and is in general the largest RS80-A measurement error at temperatures below about $-40°C$. A correction was developed for temperature-dependence error, $F(T)$ from Eq. (4), and its magnitude is about 1.1 at $-35°C$, 1.4 at $-50°C$, 1.8 at $-60°C$, and 2.5 at $-70°C$. Time-lag error results from the exponential increase in the sensor time constant with decreasing temperature. Maximum time-lag errors for conditions when the RH is changing rapidly are about $±5\%$ RH at $-20°C$, $±15\%$ RH at $-40°C$, and $±30\%$ RH at $-60°C$; typical time-lag errors are considerably less. The dependences and typical magnitudes are also given for measurement errors that result from chemical contamination of the sensor polymer, long-term sensor instability and random production uncertainty. The RS80-A, like any (unheated) solid-state sensor, is incapable of measuring ice supersaturation.

The framework was presented for an alternative correction approach that is based on understanding and correcting for the individual sources of RS80-A measurement error. A temperature-dependent correction factor was derived from the RS80-A/hygrometer dataset that corrects for the mean of all measurement errors that remain after the dataset is first corrected for the temperature-dependence error, $G'(T)$ from Eq. (5). The resulting correction for all measurement errors, $F(T) \times$

$G'(T)$, is essentially equivalent to $G(T)$. However, the approach of correcting the individual measurement errors will allow more accurate correction of individual soundings once corrections for time-lag and bias errors are completed.

We conclude overall that the Vaisala RS80-A is capable of making reliable RH measurements in the troposphere at temperatures down to $-70°C$, if corrections for well-understood measurement errors are applied. The accuracy of RS80-A measurements is substantially improved by using the corrections given in this paper, particularly at cold temperatures, and further improvement is possible and in progress.

APPENDIX A

Identifying the RS80-A Sensor

The corrections given in this paper must be applied only to Vaisala RS80-A measurements, not to measurements from the Vaisala RS80-H nor any other RH sensor. Although the Vaisala RH sensors are all subject to the same general sources of measurement error, the magnitude of the error depends strongly on the sensor type.

The RS80-A cannot be distinguished from the RS80-H based on characteristics of the data or information in the header of a sounding file. The type of RH sensor on an RS80 radiosonde can be discerned in three ways: 1) "RS80-xxxH" may (or may not) be stamped on the radiosonde if it uses the H-type sensor (where "xxx" refers to one of several possible windfinding codes), but this identification is not present on RS80-A radiosondes; 2) the RS80-H has additional coefficients on the calibration tape beginning with the letters "K" and "M" that are not present on the RS80-A calibration tape; and 3) contacting the manufacturer with the radiosonde serial number (although Vaisala cannot trace the sensor type for radiosondes manufactured before 1995).

The type of sensor can often be inferred from the date of manufacture of the radiosonde. RS80 radiosondes manufactured before 1990 will definitely use the A-type sensor, and during the years 1990–92 very few H-type sensors were used except by research programs. Prior to 1980 there were no RS80 radiosondes, and during the years 1980–84 there was overlap between the RS80-A and older radiosonde types (not RS80).

Determining the sensor type from archived data is yet

more problematic. Radiosonde data given in World Meteorological Organization (WMO) format often contain information on the type of radiosonde and sounding system. The following WMO codes correspond to Vaisala RS80 radiosondes used with various ground systems: 37 (old systems preparing messages manually), 52 (used by NWS only, and therefore RS80-H radiosondes), and 60–63 (sensor type is not discriminated). Vaisala radiosondes used with non-Vaisala ground systems (e.g., the U.S. MicroArt or French STAR systems) may include separate calculations (filtering, smoothing, etc.) that may influence the accuracy of the correction factors derived in this paper. A list of the radiosonde types used at reporting stations throughout the world is available from the WMO (at present this information is available online in the document ftp://www.wmo.ch/wmo-ddbs/OperationalInfo/RadiosondeStns/ListOfStns.xls). In general, station history information is needed in order to define with certainty the type of Vaisala RS80 sensor used.

It is an obvious recommendation that radiosonde serial numbers and sensor types be recorded in launch records for future reference and possible application of corrections.

APPENDIX B

Saturation Vapor Pressure Formulations

All of the results in this paper depend on knowing the temperature dependence of the ice-saturation curve (RH_i, the saturation humidity over ice), which is given by $RH_i(T) = e_i(T)/e_w(T)$, where e_i and e_w are the saturation vapor pressures over ice and liquid water, respectively. Numerous theoretical formulations for the saturation vapor pressures exist, several of which are summarized by Elliott and Gaffen (1991). The Goff–Gratch formulations as given in the Smithsonian Meteorological Tables (e.g., List 1968) are still in common use. However, more recent formulations may be more reliable at cold temperatures, partially because improved measurements of certain fundamental constants have become available. Few experimental measurements exist for the saturation vapor pressures at cold temperatures, but those made by Marti and Mauersberger (1993) are generally consistent with most theoretical formulations within the experimental uncertainties.

The analysis in this paper is based on the formulation for e_w given by Wexler [1976, his Eq. (15)], and the formulation for e_i given by Hyland and Wexler [1983, their Eq. (18)]. These formulations are chosen primarily because they are used by Vaisala in their sensor calibrations. The Wexler–Hyland (WH) and Goff–Gratch (GG) formulations are nearly identical for temperatures above $-40°C$, but RH_i calculated using WH is lower than that calculated using GG by 0.9% RH at $-50°C$, 1.6% RH at $-60°C$, 2.8% RH at $-70°C$, and 5.2% RH at $-80°C$. RS8O-A measurements that occur in ice-

saturated air, such as the ice-cap measurements or the similar measurements used by Vaisala to determine the temperature dependence of the calibration, will only appear to a radiosonde user to be at ice saturation if the WH formulation is used. For example, a measurement that is truly at ice saturation at $-70°C$ will appear to a user of the GG formulation to have a dry bias of 2.8% RH.

The correction factors $G(T)$ and $G'(T)$ depend on the choice of formulation because the hygrometer RH measurement is calculated from the frostpoint and air temperature measurements using the saturation vapor pressures. The temperature-dependence correction factor, $F(T)$, depends on the choice of formulation for the dual reasons that it is a function of both RH_i and $C(T)$, where $C(T)$ also depends on RH_i. The coefficients given in the paper for the functions $G(T)$, $G'(T)$, and $C(T)$ are derived using the WH formulations, and it is assumed that the reader will reference the results to the WH formulations. Because the GG formulations are in common use, we give below the coefficients for these functions derived using the GG formulations, assuming that the reader will reference the results to the GG formulations. If the reader uses a third choice for the formulations, then the corrections can be estimated by interpolating between the WH and GG results by using the values of RH_i from the three formulations to determine a scaling factor.

The coefficients for $G(T)$ in Eq. (3), derived using the GG formulation, are: $a_0 = 0.9305$, $a_1 = -5.1346 \times 10^{-3}$, $a_2 = 2.3317 \times 10^{-4}$, $a_3 = 4.0755 \times 10^{-6}$, and $a_4 = 6.3679 \times 10^{-8}$.

The coefficients for $G'(T)$ in Eq. (5), derived using the GG formulation, are: $a_0 = 0.930$, $a_1 = -4.1809 \times 10^{-3}$, $a_2 = 3.1686 \times 10^{-4}$, $a_3 = 7.2680 \times 10^{-6}$, and $a_4 = 3.0646 \times 10^{-8}$.

The coefficients for $C(T)$ in Eq. (4), derived using the GG formulation, are: $a_0 = 0.359\ 77$, $a_1 = 2.2730 \times 10^{-2}$, $a_2 = 6.3516 \times 10^{-4}$, $a_3 = -1.4476 \times 10^{-4}$, $a_4 = 6.1956 \times 10^{-7}$, and $a_5 = 1.9619 \times 10^{-8}$.

REFERENCES

Antikainen, V., and A. Paukkunen, 1994: Studies on improving humidity measurement in radiosondes: *WMO Tech. Conf. on Instruments and Methods of Observation,* Geneva, Switzerland, WMO Rep. 57, 1–5.

Balagurov, A., A. Kats, and N. Krestyannikova, 1998: Implementation and results of the WMO radiosonde humidity sensors intercomparison (Phase I laboratory test). *WMO Tech. Conf. on Meteorological and Environmental Instruments and Methods of Observation,* Casablanca, Morocco, WMO Rep. 70, 181–184.

Blackmore, W. H., and B. Taubvurtzel, 1999: Environmental chamber tests of NWS radiosonde relative humidity sensors. Preprints, *15th Int. Conf. on Interactive Information and Processing Systems (IIPS) for Meteorology, Oceanography, and Hydrology.* Dallas, TX, Amer. Meteor. Soc., 259–262.

Elliott, W. P., and D. J. Gaffen, 1991: On the utility of radiosonde humidity archives for climate studies. *Bull. Amer. Meteor. Soc.,* **72,** 1507–1520.

Gaffen, D. J., 1993: Historical changes in radiosonde instruments and

practices. Instruments and observing methods. WMO Rep. 50, 127 pp.

Heymsfield, A. J., and L. M. Miloshevich, 1993: Homogeneous ice nucleation and supercooled liquid water in orographic wave clouds. *J. Atmos. Sci.,* **50,** 2335–2353.

——, and ——, 1995: Relative humidity and temperature influences on cirrus formation and evolution: Observations from wave clouds and FIRE-II. *J. Atmos. Sci.,* **52,** 4302–4326.

——, ——, G. Sachse, C. Twohy, and S. Oltmans, 1998: Upper tropospheric relative humidity observations and implications for cirrus ice nucleation. *Geophys. Res. Lett.,* **25,** 1343–1346.

Hyland, R. W., and A. Wexler, 1983: Formulations for the thermodynamic properties of the saturated phases of H_2O from 173.15 K to 473.15 K. *ASHRAE Trans.,* **89**(2A), 500–519.

Ivanov, A., A. Kats, N. Kurnosenko, J. Nash, and N. Zaitseva, 1991: WMO International Radiosonde Intercomparison—Phase III. WMO Rep. 40, 135 pp.

Kitchen, M., 1989: Representativeness errors for radiosonde observations. *Quart. J. Roy. Meteor. Soc.,* **115,** 673–700.

List, R. J., 1968: *Smithsonian Meteorological Tables.* 6th ed. Smithsonian Institution Press, 527 pp.

Lorenc, A. C., D. Barker, R. S. Bell, B. Macpherson, and A. J. Maycock, 1996: On the use of radiosonde humidity observations in mid-latitude NWP. *Meteor. Atmos. Phys.,* **60,** 3–17.

Marti, J., and K. Mauersberger, 1993: A survey and new measurements of ice vapor pressure at temperatures between 170 and 250K. *Geophys. Res. Lett.,* **20,** 363–366.

Mastenbrook, H. J., 1968: Water vapor distribution in the stratosphere and high troposphere. *J. Atmos. Sci.,* **25,** 299–311.

Matsuguchi, M., S. Umeda, Y. Sadaoka, and Y. Sakai, 1998: Characterization of polymers for a capacitive-type humidity sensor based on water sorption behavior. *Sens. Actuators,* **49,** 179–185.

Miloshevich, L. M., and A. J. Heymsfield, 1997: A balloon-borne continuous cloud particle replicator for measuring vertical profiles of cloud microphysical properties: Instrument design, performance, and collection efficiency analysis. *J. Atmos. Oceanic Technol.,* **14,** 753–768.

Oltmans, S. J., and D. J. Hofmann, 1995: Increase in lower strato-

spheric water vapour at a mid-latitude Northern Hemisphere site from 1981 to 1994. *Nature,* **374,** 146–149.

Paukkunen, A., 1995: Sensor heating to enhance reliability of radiosonde humidity measurement. Preprints, *11th Int. Conf. on Interactive Information and Processing Systems for Meteorology, Oceanography, and Hydrology,* Dallas, TX, Amer. Meteor. Soc., 103–106.

Ross, R. J., and W. P. Elliott, 1996: Tropospheric water vapor climatology and trends over North America: 1973–93. *J. Climate,* **9,** 3561–3574.

Sakai, Y., Y. Sadaoka, and M. Matsuguchi, 1996: Humidity sensors based on polymer thin films. *Sens. Actuators,* **35,** 85–90.

Salasmaa, E., and P. Kostamo, 1975: New thin film humidity sensor. Preprints, *Third Symp. on Meteorological Observations and Instrumentation,* Washington, DC, Amer. Meteor. Soc., 33–38.

Schmidlin, F. J., and A. Ivanov, 1998: Radiosonde relative humidity sensor performance: The WMO intercomparison–Sept 1995. Preprints, *10th Symp. on Meteorological Observations and Instrumentation,* Phoenix, AZ, Amer. Meteor. Soc., 68–71.

Semerjian, H. G., 1990: Report of calibration on twenty radiosonde humidity sensors (H-Humicap). NIST Rep. TN245604, 12 pp.

Soden, B. J., and J. R. Lanzante, 1996: An assessment of satellite and radiosonde climatologies of upper-tropospheric water vapor. *J. Climate,* **9,** 1235–1250.

——, S. A. Ackerman, D. O'C. Starr, S. H. Melfi, and R. A. Ferrare, 1994: Comparison of upper tropospheric water vapor from GOES, Raman lidar, and cross-chain loran atmospheric sounding system measurements. *J. Geophys. Res.,* **99,** 21 005–21 016.

Vömel, H., S. J. Oltmans, D. J. Hofmann, T. Deshler, and J. M. Rosen, 1995: The evolution of the dehydration in the Antarctic stratospheric vortex. *J. Geophys. Res.,* **100,** 13 919–13 926.

Wade, C. G., 1995: Calibration and data reduction problems affecting national weather service radiosonde humidity measurements. Preprints, *Ninth Symp. on Meteorological Observations and Instrumentation,* Charlotte, NC, Amer. Meteor. Soc., 37–42.

Wexler, A., 1976: Vapor pressure formulation for water in range 0 to 100°C: A revision. *J. Res. Nat. Bur. Stand.,* **80A,** 775–785.

WMO, 1996: Measurements of upper air temperature, pressure, and humidity. *Guide to Meteorological Instruments and Methods of Observation,* 6th ed., WMO I.12-1–I.12-32.